

Understanding the relative importance of magnetic field, gravity, and turbulence in star formation at the hub of the giant molecular cloud G148.24+00.41

Vineet Rawat,^{1,2*} M. R. Samal,¹ Chakali Eswaraiah,³ Jia-Wei Wang,⁴ Davide Elia,⁵ Sandhyarani Panigrahy,³ A. Zavagno,^{6,7} R. K. Yadav,⁸ D. L. Walker,⁹ J. Jose,³ D.K. Ojha,¹⁰ C.P. Zhang,^{11,12} S. Dutta,⁴

¹Physical Research Laboratory, Navrangpura, Ahmedabad, Gujarat 380009, India

²Indian Institute of Technology Gandhinagar Palaj, Gandhinagar 382355, India

³Indian Institute of Science Education and Research (IISER) Tirupati, Rami Reddy Nagar, Karakambadi Road, Mangalam (P.O.), Tirupati 517 507, India

⁴Academia Sinica Institute of Astronomy and Astrophysics, No.1, Sec. 4, Roosevelt Road, Taipei 10617, Taiwan

⁵Istituto di Astrofisica e Planetologia Spaziali, INAF, Via Fosso del Cavaliere 100, I-00133 Roma, Italy

⁶Aix-Marseille Universite, CNRS, CNES, LAM, 38 rue F. Joliot Curie, F-13388 Marseille Cedex 13, France

⁷Institut Universitaire de France, Paris, 1 rue Descartes, F-75231 Paris Cedex 05, France

⁸National Astronomical Research Institute of Thailand (NARIT), Sirindhorn AstroPark, 260 Moo 4, T. Donkaew, A. Maerim, Chiangmai 50180, Thailand

⁹Jodrell Bank Centre for Astrophysics, Department of Physics and Astronomy, University of Manchester, Oxford Road, Manchester M13 9PL, UK

¹⁰Department of Astronomy and Astrophysics, Tata Institute of Fundamental Research, Mumbai 400005, India

¹¹National Astronomical Observatories, Chinese Academy of Sciences, Beijing 100101, People's Republic of China

¹²Guizhou Radio Astronomical Observatory, Guizhou University, Guiyang 550000, People's Republic of China

11 January 2024

ABSTRACT

The relative importance of magnetic fields, turbulence, and gravity in the early phases of star formation is still not well understood. We report the first high-resolution dust polarization observations at 850 μm around the most massive clump, located at the hub of the Giant Molecular Cloud G148.24+00.41, using SCUBA-2/POL-2 at the James Clerk Maxwell Telescope. We find that the degree of polarization decreases steadily towards the denser portion of the cloud. Comparing the intensity gradients and local gravity with the magnetic field orientations, we find that local gravity plays a dominant role in driving the gas collapse as the magnetic field orientations and gravity vectors seem to point towards the dense clumps. We also find evidence of U-shaped magnetic field morphology towards a small-scale elongated structure associated with the central clump, hinting at converging accretion flows towards the clump. Our observation has resolved the massive clump into multiple substructures. We study the magnetic field properties of two regions, central clump (CC) and northeastern elongated structure (NES). Using the modified Davis-Chandrasekhar-Fermi method, we determine that the magnetic field strengths of CC and NES are $\sim 24.0 \pm 6.0 \mu\text{G}$ and $20.0 \pm 5.0 \mu\text{G}$, respectively. The mass-to-flux ratios are found to be magnetically transcritical/supercritical, while the Alfvén Mach number indicates a trans-Alfvénic state in both regions. These results, along with Virial analysis, suggest that at the hub of G148.24+00.41, gravitational energy has an edge over magnetic and kinetic energies.

Key words: ISM: clouds; ISM: magnetic fields; polarization; galaxies: star clusters: general, ISM: molecules; molecular data

1 INTRODUCTION

Molecular clouds, the enigmatic birthplaces of stars, are now well established to consist of filamentary structures, revealed by *Herchel* observations (Molinari et al. 2010; André et al. 2013; Zavagno et al. 2023). Within these immense structures of cold gas and dust, the gravity, turbulence, and magnetic fields dictate the process of star formation at different scales, from large scale (cloud and filaments) to small scale (clumps and dense cores) (Klessen et al. 2000; Ballesteros-

Paredes et al. 2007; Federrath 2015; Tang et al. 2019; Wang et al. 2020b; Pattle et al. 2022). However, their relative role during the different stages of cloud evolution is still unclear and a topic of debate (Li et al. 2014).

The magnetic field exists throughout star-forming molecular clouds across various scales (see the review article by Pattle et al. 2022) and plays a crucial role in the formation of molecular clouds and filamentary structures (Soler et al. 2013; Hennebelle & Inutsuka 2019). Numerical simulations show that the strong magnetic fields play an important role in the magnetically channelled gravitational collapse of clouds (Nakamura & Li 2008; Gómez et al. 2018), and

* E-mail: vineet@prl.res.in

can channel turbulent flows along the filaments (Li & Houde 2008; Soler et al. 2013; Zamora-Avilés et al. 2017), guide the accreting matter (Seifried & Walch 2015; Shimajiri et al. 2019), and dynamically influence the formation of cores along the dense ridges of the filamentary clouds (e.g. Koch et al. 2014; Zhang et al. 2014; Cox et al. 2016; Pattle et al. 2017; Soam et al. 2018; Liu et al. 2019; Eswaraiah et al. 2021). At parsec (or few parsec) scale, the magnetic field typically shows an ordered structure, mostly aligned with the long axis of the low-density elongated gas structures such as striations, while in high-density filaments, the magnetic field lines are preferentially perpendicular to the long axes of filaments (e.g. Cox et al. 2016; Planck Collaboration et al. 2016; Soler et al. 2017; Ward-Thompson et al. 2017; Tang et al. 2019; Soam et al. 2019; Doi et al. 2020). At sub-parsec scales, the magnetic field can be very complex depending upon the turbulent nature of the magnetic field and stellar feedback (e.g. Hull et al. 2017; Eswaraiah et al. 2020; Eswaraiah et al. 2021). Dust polarization studies at small scales have revealed a variety of magnetic field morphologies in dense clumps and cores, and the results suggest that the magnetic field is scale-dependent and varies with the environment (e.g. Girart et al. 2013; Hull et al. 2017; Ward-Thompson et al. 2017; Pattle et al. 2018; Eswaraiah et al. 2020; Eswaraiah et al. 2021).

Moreover, it is not clear whether it is turbulence or magnetic field along with gravity that dominates the star formation process. The role of gravity has long been recognised as the primary factor driving the collapse of dense regions and initiating the birth of protostellar cores. On the other hand, turbulence, the chaotic and ubiquitous motion of gas within these massive clouds, influences the fragmentation of the collapsing gas. However, the role of magnetic field, in comparison to turbulence and gravity, is relatively less understood at various stages of star formation.

The “strong magnetic field” theory of star formation stresses the importance of the magnetic field in the formation and evolution of clouds and subsequent structures (Mouschovias et al. 2006; Tan et al. 2013; Hennebelle 2018). Conversely, the “weak magnetic field” theory suggests that turbulent flows control the formation and evolution of clouds and cores, and create the compressed regions where stars form (Padoan & Nordlund 2002; Mac Low & Klessen 2004; Federrath & Klessen 2012). Observationally also, in some high-mass star-forming regions, it has been found that the turbulent energy is more dominant or comparable to magnetic energy (e.g. Beuther et al. 2010; Girart et al. 2013; Beuther et al. 2020; Wang et al. 2020b). In contrast, other studies found magnetic energy to be more dominant than turbulent energy (e.g. Girart et al. 2009; Beuther et al. 2018; Eswaraiah et al. 2020; Chung et al. 2023). Therefore, more observational evidence is required at the early stages of star formation to better constrain the theoretical models and relative roles of gravity, magnetic field, and turbulence in the star-forming regions.

Dust polarization observation is a key tool for tracing the plane-of-sky (POS) magnetic field geometry in star-forming regions. The polarization is caused by asymmetric dust grains that preferentially align their shorter axis along the magnetic field direction (Lazarian 2007; Hoang & Lazarian 2008). There are different mechanisms for dust grain alignment (see the review article by Andersson et al. 2015), but the most widely accepted one being is the radiative alignment torque (RAT) mechanism (Lazarian 2007; Hoang & Lazarian 2014; Andersson et al. 2015).

Located at a distance of ~ 3.4 kpc, G148.24+00.41 is a massive cloud having mass $\sim 10^5 M_{\odot}$ and dust temperature ~ 14.5 K, and it resembles a hub-filament morphology (Rawat et al. 2023). The cloud is still at the early stages of its evolution such that the stellar feedback mechanisms like stellar winds and expanding H II regions are not

yet significant (Rawat et al. 2023), which makes G148.24+00.41 a potential candidate to study the early stages of the star and cluster formation process. Fig. 1a shows the ^{13}CO intensity map of G148.24+00.41, integrated in the velocity range of -37.0 km s $^{-1}$ to -30.0 km s $^{-1}$, where one can see a bright spot in the centre of the map. This location corresponds to the most massive clump of the cloud, which is nomenclatured as C1 in Rawat et al. (2024). Rawat et al. (2024), using CO molecular data (spatial resolution $\sim 52''$ or 0.9 pc at distance ~ 3.4 kpc, velocity resolution ~ 0.17 km s $^{-1}$), also found filamentary features and seven massive clumps in G148.24+00.41. The C1 clump with a mass of $\sim 2100 M_{\odot}$ and an effective size of ~ 1.8 pc based on C ^{18}O data, is found to be at the hub/central location of the cloud. The filamentary features attached to the C1 clump can also be seen in *Herschel* 250 μm image, shown in Fig. 1b (adapted from Rawat et al. 2023). The figure clearly reveals the hub-filament system morphology of the cloud. Rawat et al. (2023) found that the clump hosts an infrared cluster, seen in *Spitzer* bands, and hypothesised that the cluster might grow to a richer cluster by accumulating gas from the extended reservoir. Such hub filamentary systems with the clump being located at the nexus or junction of these filaments are of particular interest because these are the sites where cluster formation would take place, as advocated in simulations and observations (e.g. Naranjo-Romero et al. 2012; Gómez & Vázquez-Semadeni 2014; Gómez et al. 2018; Vázquez-Semadeni et al. 2019; Kumar et al. 2020).

The magnetohydrodynamic simulations suggest that the filamentary converging flows would impact the magnetic field morphology of the star-forming regions (Gómez et al. 2018). In G148.24+00.41, Rawat et al. (2024) found converging gas flows along the filaments towards the hub. So, it would be interesting to investigate the influence of gas flows on the B-field morphology in the hub of the cloud. In addition, it is equally important to examine the role of magnetic fields in the stability of such hub systems, as it is expected that gravity would play a dominant role in the onset of star formation within such systems. In this work, we investigate the morphology and strength of the magnetic field of the C1 clump of G148.24+00.41 for the first time, in order to understand the relative importance of the magnetic field in comparison to gravity and turbulence in the overall star formation process of the clump. This paper is organised as follows. In Section 2, we describe the observations, data reduction, and other data sets used in this work. In Section 3, we present the analysis and results related to the magnetic field morphology, its relative orientation in comparison to intensity gradients and local gravity, and its strength. We also discuss the dust and gas properties of the studied region. In Section 4, we discuss the results and compare the strength of gravity, magnetic field, and turbulence. In Section 5, we summarize the findings of this work.

2 OBSERVATIONS AND DATA

2.1 Dust continuum polarization observations using JCMT SCUBA-2/POL-2

We observed the C1 clump/hub region of G148.24+00.41 with SCUBA-2/POL-2 mounted on the James Clerk Maxwell Telescope (JCMT), a single-dish sub-millimeter telescope in Mauna Kea, Hawaii, USA. The POL-2 instrument is a linear polarimetry module (Friberg et al. 2016) for the Submillimetre Common User Bolometer Array-2 (SCUBA-2), a 10,000 bolometer camera on the JCMT (Holland et al. 2013). The data was acquired between 2022 November 25 and 2023 January 03 (project code: M22BP055; PI: Vineet

Rawat) in the band 2 weather conditions under an atmospheric optical depth at 225 GHz (τ_{225}) of 0.04 to 0.06. The observations were taken in 10 sets with an integration time of 30 minutes each, resulting in a total integration time of around 5.5 hr. The POL-2 DAISY scan mode (Holland et al. 2013; Friberg et al. 2016) was adopted, which generates a map of high signal-to-noise ratio (SNR) within a central region spanning a diameter of 3', and the noise level gradually increases towards the edges of the map. The region is observed in both the 450 and 850 μm continuum polarizations simultaneously, with a resolution of 9''6 and 14''1, respectively. Due to the low sensitivity of the 450 μm data, this paper presents the analyses and results based on only 850 μm dust polarization data.

The data reduction was carried out using the *pol2map*¹ script in the SMURF package (Chapin et al. 2013) of Starlink (Currie et al. 2014). The POL-2 is characterized by linear polarization that produces Stokes I, Q, and U vector maps. The *Skyloop* mode was utilised to minimise the uncertainty associated with map creation, while the MAPVARS mode was enabled to assess the total uncertainty from the standard deviation among individual observations. The details of the data reduction process of POL-2 can be found in Pattle et al. (2017) and Wang et al. (2019). Finally, the I, Q, and U maps, along with their variance maps, are used to create a debiased polarization vector catalogue. The catalogue consists of total intensity (I), Stokes vectors (Q and U), polarization intensity (PI), polarization fraction (P), polarization angle (θ_P), and their associated uncertainties (δI , δQ , δU , δPI , δP , and $\delta\theta_P$, respectively).

The I, Q, and U maps are produced with 4'' pixel size, while the polarization catalogue is binned to 12'', for better sensitivity. A flux calibration factor of 668.25 Jy beam⁻¹ pW⁻¹ is used for 850 μm Stokes I, Q, and U map to convert them from pW to mJy/beam and to account for the flux-loss due to POL-2 insertion into the telescope. This calibration factor comprises 495 Jy/beam/pW for reductions using 4'' pixels of SCUBA-2, multiplied by the standard 1.35 factor for POL-2 losses (Mairs et al. 2021).

The polarised intensity is defined to be positive, so the uncertainties of the Q and U Stokes vector would bias the polarised intensities towards larger values (Vaillancourt 2006; Kwon et al. 2018). The debiased polarization intensity and its uncertainty are calculated as

$$PI = \sqrt{Q^2 + U^2 - 0.5(\delta Q^2 + \delta U^2)} \quad (1)$$

and

$$\delta PI = \sqrt{\frac{(Q^2 \delta Q^2 + U^2 \delta U^2)}{(Q^2 + U^2)}},$$

respectively. The debiased polarization fraction and its uncertainty are then calculated as

$$P = \frac{PI}{I} \quad (2)$$

and

$$\delta P = \sqrt{\frac{\delta PI^2}{I^2} + \frac{\delta I^2 (Q^2 + U^2)}{I^4}},$$

respectively. The polarization angle and its uncertainty are calculated as

$$\theta_P = \frac{1}{2} \tan^{-1} \left(\frac{U}{Q} \right) \quad (3)$$

and

$$\delta\theta_P = \frac{1}{2} \sqrt{\frac{(U^2 \delta Q^2 + Q^2 \delta U^2)}{(Q^2 + U^2)^2}},$$

respectively. The polarization angle increases from the north toward the east, following the IAU convention. The mean rms noises in the Stokes I, Q, U, and PI measurements with 12'' bin size are 1.4, 1.1, 1.1, and 1.1 mJy beam⁻¹, respectively. Following the standard convention, for magnetic field, hereafter, B-field orientations, the polarization angles are rotated by 90 degrees.

2.2 Molecular line data from PMO

We used the ¹³CO (J = 1–0) and C¹⁸O (J = 1–0) molecular line data, which were taken as a part of the Milky Way Imaging Scroll Painting survey (MWISP; Su et al. 2019) using the 13.7-m radio telescope at Purple Mount Observatory (PMO). The observation of CO isotopologues was taken simultaneously using a 3 × 3 beam sideband-separating Superconducting Spectroscopic Array Receiver (SSAR) system (Shan et al. 2012) and using the position-switch on-the-fly mode. The spatial resolution (Half Power Beam Width; HPBW) of ¹³CO and C¹⁸O is around ~52'' (~0.9 pc at 3.4 kpc). And the spectral resolution of ¹³CO and C¹⁸O is ~0.17 km s⁻¹ with a sensitivity of ~0.3 K (for details, see Su et al. 2019).

3 ANALYSES AND RESULTS

Fig. 1c shows the Stokes I map of the region, where the location of the C1 clump is also shown. From the figure, it can be seen that the 850 μm JCMT data (beam size ~14'') has resolved multiple sub-structures in the central region of the cloud. We found sub-structures like a central clump, a clump located on the western side, and a prominent elongated structure on the northeastern side of the central clump. In addition to these prominent sub-structures, a few compact structures are also visible in the image.

3.1 B-field morphology

In order to select the significant polarization detections, we set the following criteria for selecting data: $I/\delta I > 10$, $P/\delta P > 2$, and $P < 30\%$. By doing this, we got 69 polarization measurements in our target region. The P values range from ~2 % to ~29 % with a mean and standard deviation around $\sim 11 \pm 8$ %. The B-field orientations are widely distributed, ranging from ~6° to 180° with a mean and standard deviation around $\sim 91^\circ \pm 48^\circ$, suggesting a complex B-field morphology in the region. The mean uncertainties in polarization fraction and polarization angle are ~3.5% and ~9°, respectively. Fig. 2a and b show the distribution of polarization vectors and B-field orientations, respectively, over the 850 μm Stokes I dust continuum emission map of the region. The contour levels in the map are shown above 3 σ from the background, where σ is the mean rms noise (5 mJy beam⁻¹) of the Stokes I map.

In this work, based on 850 μm Stokes I intensity and magnetic field orientations, we defined the central clump, clump located on the

¹ <http://starlink.eao.hawaii.edu/docs/sc22.htx/sc22.html>

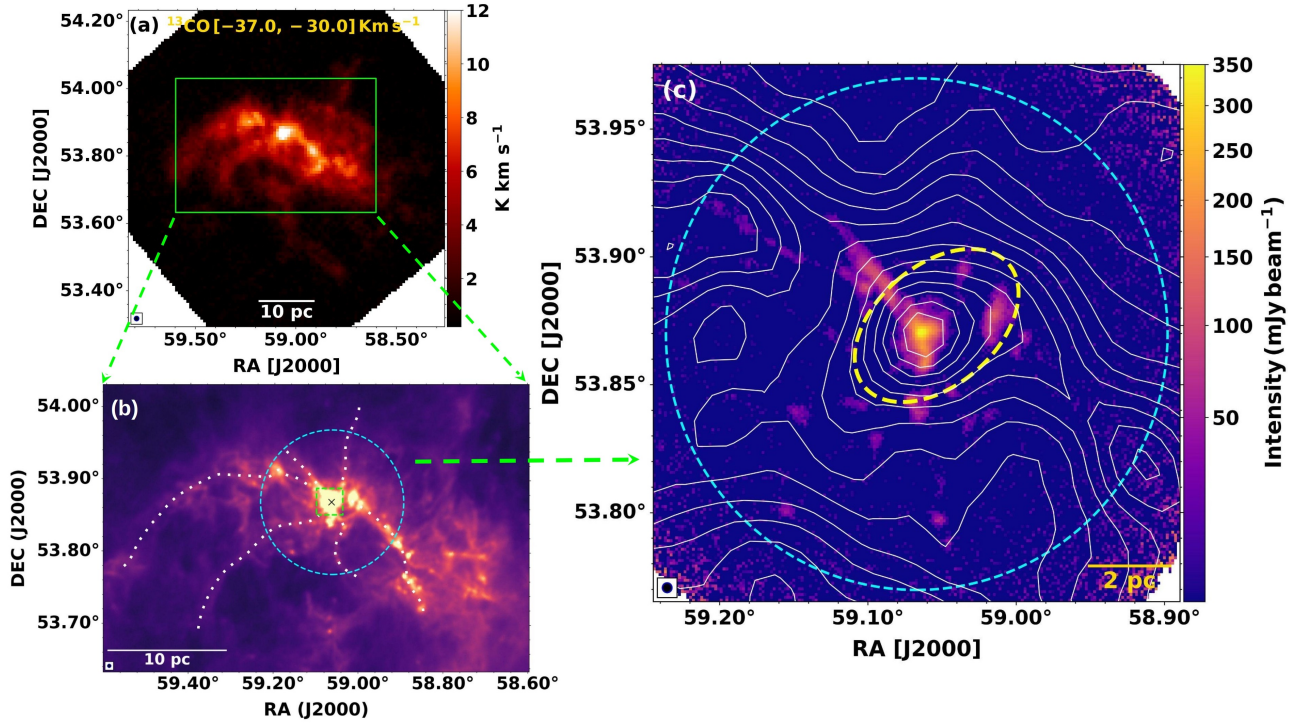


Figure 1. (a) ^{13}CO ($J = 1-0$) intensity map of G148.24+00.41, integrated in the velocity range -37.0 km s^{-1} to -30.0 km s^{-1} . (b) The central region (encompassed by the solid green box in panel-a) of G148.24+00.41 as seen in *Herschel* $250 \mu\text{m}$ band, showing the hub-filamentary morphology of the cloud. The figure is adapted from Rawat et al. (2023), in which the blue circle shows the JCMT scanned region of diameter $\sim 12'$ ($\sim 12 \text{ pc}$). The green dashed box marks the central area of the hub, where an infrared cluster is seen (Rawat et al. 2023), and the cross sign indicates the position of a massive young stellar object. (c) The $850 \mu\text{m}$ Stokes I intensity map of the central region of G148.24+00.41 mapped by JCMT SCUBA-2/POL-2, along with the contours of ^{13}CO integrated intensity emission, drawn from 1.5 to 15 K km s^{-1} with a step size of $\sim 0.96 \text{ K km s}^{-1}$. The rms noise of the $4''$ pixel-size Stokes I map is around $\sim 5 \text{ mJy beam}^{-1}$. In panel-c, the yellow ellipse shows the position of the C1 clump, identified by Rawat et al. (2024) using C^{18}O data (spatial resolution $\sim 52''$). The beam sizes of the ^{13}CO integrated intensity map, *Herschel* $250 \mu\text{m}$ map, and JCMT $850 \mu\text{m}$ map are $\sim 52''$, $18''$, and $14''$, respectively, shown as a framed-blue dot at the bottom left of each panel.

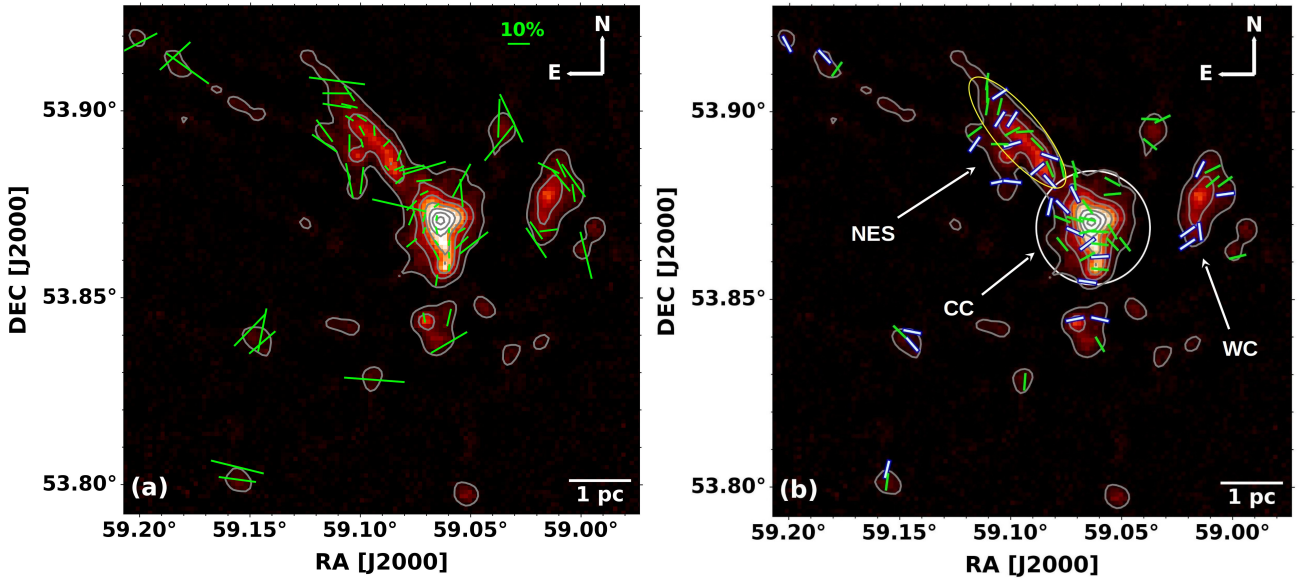


Figure 2. (a) Polarization vector map with lengths proportional to polarization fraction, and (b) magnetic field orientation map with fixed lengths. The background is the Stokes I image at $850 \mu\text{m}$, and the contour levels are drawn at 3σ above the rms noise level of 5 mJy beam^{-1} , starting from 15 mJy beam^{-1} to $300 \text{ mJy beam}^{-1}$. The segments shown are binned to a $12''$ pixel grid and correspond to polarization data with $I/\delta I > 10$ and $P/\delta P > 2$. The lightcyan and green vectors in panel-b show the measurements with $2 < P/\delta P < 3$ and $P/\delta P > 3$, respectively. The regions used for B-field calculation are also shown in panel-b by a white circle and yellow ellipse for the CC and NES, respectively.

western side, and northeastern elongated structure as CC, WC, and NES, respectively, as marked in Fig. 2b. The approximate extents of these regions are defined by considering the outermost closed contours of the 850 μm Stokes I map. From Fig. 2b, it can be seen that the B-field orientations in the CC are mostly oriented along the east-west direction (PA $\sim 90^\circ$), while some of them are at smaller position angles. There exist mixed B-field orientations in the NES region, some in the low-density area are nearly perpendicular to the major axis of the NES, while some closer to the CC are parallel to it. In the WC, most of the B-fields are converging towards the centre, aligned along the southeast direction, which may be influenced by gravity (see Section 3.3.2 and 4.1). Overall, the B-field morphology around the central region of G148.24+00.41 is complex, which is probably due to hierarchical fragmentation and a network of filamentary flows towards the hub, as found by Rawat et al. (2023) and Rawat et al. (2024).

Fig. 3a shows the histogram of the B-field orientations in the central region of G148.24+00.41, which is broadly distributed. The CC is showing mixed morphology, having two peaks, one at $\sim 38^\circ$ (i.e. with position angles close to northeast), and the second is at $\sim 80^\circ$ (i.e. with position angles parallel to east). The NES shows a flat distribution over a broad range, but a slightly higher distribution at a position angle around $\sim 180^\circ$. The WC, though, has a small number of segments, shows a peak around $\sim 125^\circ$, i.e. mostly in the southeast direction. All these orientations are also clearly evident in Fig. 3b, which shows the distribution of B-field position angles. From Fig. 3b, it can be seen that the B-field angles change roughly from $\sim 180^\circ$ to $\sim 70^\circ$ while going from the elongated structure towards the central clump.

3.2 Variation of polarization fraction: depolarization effect

Fig. 4 shows the distribution of polarization fraction over the contours of Stokes I emission. From the figure, it can be seen that the polarization fraction is lower in the high-intensity regions compared to the low-intensity regions, which shows the decreasing trend of polarization fraction with the total intensity, known as depolarization. The depolarization effect has been reported in several studies (Girart et al. 2006; Tang et al. 2013; Sadavoy et al. 2018; Soam et al. 2018; Liu et al. 2019, 2020), and is mainly explained by the inefficient radiative alignment of dust grains in high-density regions or integration effect across a complex magnetic fields. In high-density regions, the radiative alignment torques decrease due to the attenuation of interstellar radiation that results in poor grain alignment, and hence the decrease in polarization fraction. However, the grain characteristics like size, shape, composition, and grain growth can also affect the dust grain alignment. The turbulent nature of the B-field and unresolved complex and tangled B-fields within the JCMT beam, being averaged across the beam, can also give low dust polarization (Planck Collaboration et al. 2016, 2020). We want to point out that in the hub/CI clump of G148.24+00.41, supersonic non-thermal motions have been found (sonic Mach number = 3–4.4, see Rawat et al. (2024)). Therefore, the turbulent nature of the B-field can also be the cause of depolarization in our target.

The relation between polarization fraction and intensity is expected to follow a power-law, $P \propto I^{-\alpha}$ (Whittet et al. 2008). A range of α values has been found in molecular clouds from ~ 0.5 to 1 (Chung et al. 2023, and references therein). The α value is often used as an indicator of the dust grain alignment efficiency. When $\alpha = 0$, it implies a constant grain alignment efficiency, $\alpha = 0.5$ implies that the alignment decreases linearly with the increasing optical depth,

while $\alpha = 1$ implies an alignment limited to the outer regions of the cloud, and at higher density, there is no preferred alignment of grains relative to the magnetic field (Whittet et al. 2008). We fit the P-I relation with a single power-law (weighted-fit) and found an index, $\alpha = 0.95 \pm 0.04$, which shows that the dust grain alignment efficiency is decreasing in the central dense region of G148.24+00.41. However, Pattle et al. (2019) shows that the conventional approach of fitting a single power-law over the polarization measurements debiased with Gaussian noise is only applicable above a high SNR cut. But in low polarized intensity regions, a high SNR would discard more data, and therefore, the α index will be overestimated (Pattle et al. 2019; Chung et al. 2023; Lin et al. 2023). Wang et al. (2019) also found that the value of α depends upon the cut of SNR and tends to -1 if we put a constraint on $P/\delta P$. Hence, to obtain the true value of the α index, it is recommended to use the non-debiased polarization measurements, including both the low and high SNR data, and should not put constraints on $P/\delta P$ (Pattle et al. 2019; Wang et al. 2019).

We followed the Bayesian method of Wang et al. (2019) to determine the true value of α by using the non-debiased polarization data, which follows well the Rice distribution (see Pattle et al. 2019; Wang et al. 2019, and references therein)

$$F(P|P_0) = \frac{P}{\sigma_P^2} \exp\left[-\frac{P^2 + P_0^2}{2\sigma_P^2}\right] I_0\left(\frac{PP_0}{\sigma_P^2}\right), \quad (4)$$

where P and P_0 are the observed and true polarization fraction, respectively, σ_P is the uncertainty in the polarization fraction, and I_0 is the zeroth-order modified Bessel function. We used non-debiased data with an SNR of 2 (i.e. $I/\delta I > 2$) to include most of the data points and used the power-law model, $P_0 = \beta I^{-\alpha}$, with uncertainty $\sigma_P = \sigma_{QU}/I$, where σ_{QU} represents the rms noise in Q and U measurements, I is the total observed intensity, and α , β , and σ_{QU} are the free model parameters. We employed the Markov Chain Monte Carlo method and used a python package PyMC3 (Salvatier et al. 2016) to fit the Rician model to the data. We set the uniform priors on all three model parameters: $0 < \alpha < 2$, $0 < \beta < 100$, and $0 < \sigma_{QU} < 5$, and otherwise a value of 0 for all the parameters. The details of the methodology are given in Wang et al. (2019). Fig. 5 shows the derived posterior of each model parameter, along with their 95% highest density interval (HDI), depicting the uncertainty in each parameter. The mean values of α , β , and σ_{QU} are ~ 0.6 , 37, and 1.7, respectively. The α value derived from the non-debiased polarization data is smaller than the α value derived from the conventional approach (i.e. ~ 0.95). Fig. 6 shows the non-debiased polarization fraction versus total intensity plot with 50%, 68%, and 95% confidence interval. The derived α value suggests that the grain alignment is still persisting in the hub of G148.24+00.41, but with decreasing efficiency in the dense regions.

3.3 Relative orientations of magnetic fields, intensity gradients, and local gravity

In star-forming regions, various forces interact, like gravity, magnetic field, and turbulence, which shape the geometry of these regions and drive the star-formation process (Ballesteros-Paredes et al. 2007; Koch et al. 2012a; Pattle et al. 2022). Along with the overall strength of these individual factors for an entire region (discussed in Section 4.2), it is also important to investigate their localised relative orientations in the map, as it would give insight into the localised effect of these factors (Koch et al. 2012a,b, 2013; Tang et al. 2019; Liu et al. 2020; Wang et al. 2020b). Koch et al. (2012a) developed a technique,

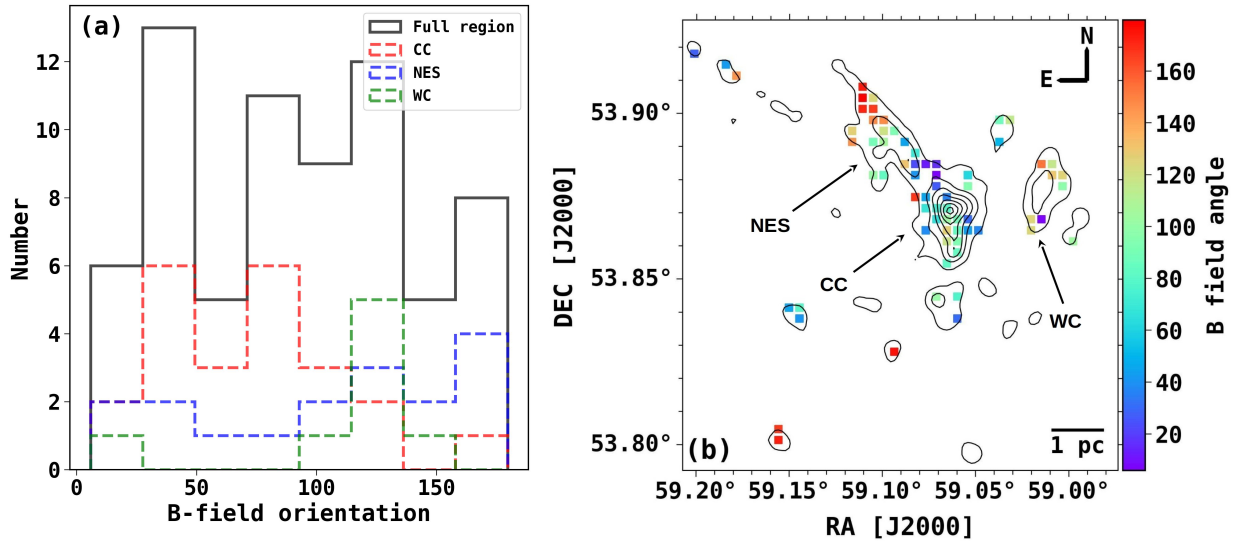


Figure 3. (a) Histogram of B-field position angles for the whole region, CC, NES, and WC. (b) Distribution of B-field position angles over the contours of 850 μm Stokes I map. The contour levels are the same as in Fig. 2.

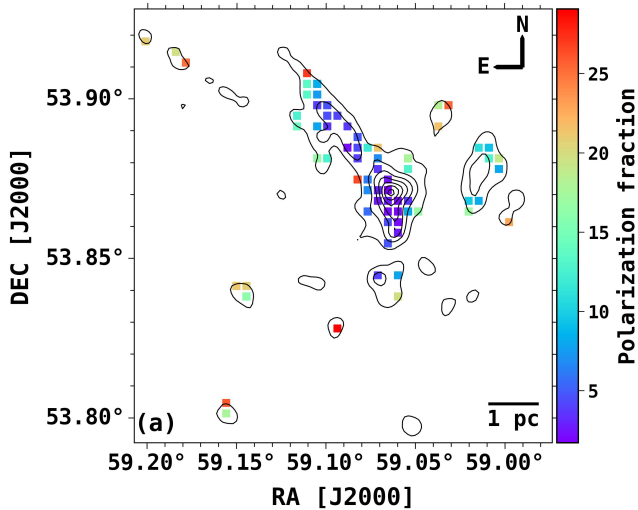


Figure 4. Distribution of dust polarization fraction (P in %) over the contours of 850 μm Stokes I map. The contour levels are the same as in Fig. 2.

"the polarization-intensity gradient-local gravity," using Magnetohydrodynamics (MHD) force equations to measure the local magnetic field strengths. Following the approach of Koch et al. (2012a,b), we find out the angular difference between magnetic field, intensity gradient, and local gravity, and discuss their relative importance at different positions.

3.3.1 Intensity gradient versus magnetic field

We used the 850 μm dust continuum intensities of all pixels in the map to determine the directions of intensity gradients. All the pixels that have values above a certain threshold (i.e. 3σ above the mean rms noise in the Stokes I map) are considered for computing the direction of gradients, except those that exist at the edges. For a pixel at position (α_i, δ_j) , the position angle (θ'_{IG}) of the intensity gradient is calculated as

$$\theta'_{IG} = (180/\pi) \times \arctan \left[\frac{\Delta I_{\delta_j}}{\Delta I_{\alpha_i}} \right], \quad (5)$$

where $\Delta I_{\delta_j} = I_{\delta_{j+1}} - I_{\delta_{j-1}}$ and $\Delta I_{\alpha_i} = I_{\alpha_{i+1}} - I_{\alpha_{i-1}}$.

The θ'_{IG} values are then converted to gradient directions (θ_{IG}) by doing the quadrant corrections, i.e. arranging the angles between 0° and 360° (for details, see Eswaraiah et al. 2020). In order to plot the gradient orientations instead of directions, we folded the θ_{IG} between 0° and 180° . For comparison of the gradient orientations (θ_{IG}) with the B-field orientations (θ_B), we took the average of all the θ_{IG} values within a diameter of $\sim 14''$ (corresponds to the beam size of JCMT at 850 μm) around each B-field position. We calculated the circular mean to get the average of intensity gradients. In this approach, the angles are treated as unit vectors, which is adequate for broad distributions and ambiguity in angles (Tang et al. 2019). Fig. 7a shows the orientations of intensity gradients relative to B-field orientations over the 850 μm Stokes I map.

We find that the local differences between these orientations are overall widely distributed. However, it can be seen that the intensity gradients are mostly aligned with the B-fields in the CC and WC regions, while the differences in orientations are relatively higher in the NES region. In the observed central region of G148.24+00.41, we found a moderate correlation between θ_B and θ_{IG} , in the CC and WC (see Figs. 7a, b). Fig. 7b shows the distribution of $\Delta\theta_{B,IG} = |(\theta_B - \theta_{IG})|$ over the contours of 850 μm Stokes I map. The $\Delta\theta_{B,IG}$ values lie between 0° and 90° after considering them to be the acute angle. A stronger correlation between θ_B and θ_{IG} tells that the material is following the B-field lines (Koch et al. 2013; Tang et al. 2019, more discussion in Section 4.1).

3.3.2 Local gravitational field versus magnetic field

In order to investigate the localised effect of gravity on the B-field morphology of the structures, we used the 850 μm dust continuum map, to compute the projected gravitational field vectors. The gravitational force at any pixel ($F_{G,i}$) is the vector sum of the forces from all the surrounding pixels and is expressed as (Wang et al. 2020b).

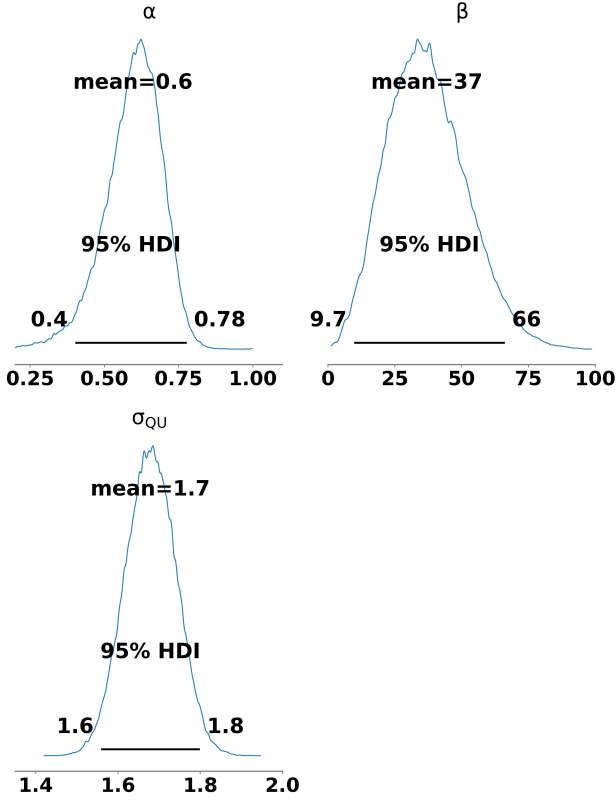


Figure 5. The probability distribution function of the fitted model parameters derived using the Bayesian method over the non-debiased polarization data. The mean values of the parameters are shown along with the 95% HDI intervals to represent the uncertainties. The 95% confidence intervals are marked as horizontal bars.

$$F_{G,i} = k I_i \sum_{j=1}^N \frac{I_j}{r_{ij}^2} \hat{r}, \quad (6)$$

where I_i and I_j are the intensity of the pixel at position i and j , respectively, and k is the term that takes care of the conversion of emission to total column density and also includes the gravitational constant. N is the total number of pixels within the selected area, r_{ij} is the projected distance between the pixels i and j , and \hat{r} is the unit vector. Considering only the directions of the local gravitational forces, we take k to be 1 in the above equation by assuming that the spatial distribution of dust will be analogous to the spatial distribution of mass. Similar to the intensity gradient map, we selected those pixels which have intensity values above the threshold, and obtained the local gravity vectors (θ_{LG}) at each B-field position, by taking an average of all vectors within the $14''$ beam size. Fig. 8a shows the orientations of local gravity vectors relative to B-field orientations over the $850 \mu\text{m}$ Stokes I map. From the figure, it can be seen that similar to intensity gradients, the local gravity vectors are also mostly aligned with the B-fields in the CC and WC region, whereas they deviate from the B-fields in the NES region. Fig. 8b shows the distribution of $\Delta\theta_{B,LG} = |(\theta_B - \theta_{LG})|$ values over the contours of $850 \mu\text{m}$ Stokes I emission, which are treated to be acute angles.

The relative orientations of intensity gradient and local gravity have a similar distribution like that of $\Delta\theta_{B,IG}$ and $\Delta\theta_{B,LG}$, as shown in Fig. A1 in appendix A. Figs. 9a-c shows the histogram

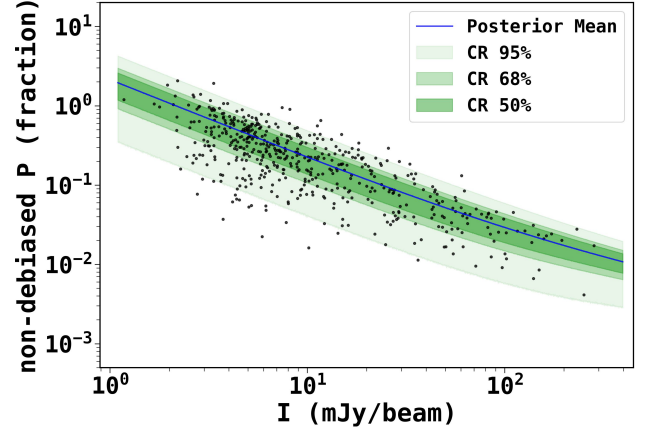


Figure 6. Non-debiased polarization fraction versus total intensity. The blue line shows the mean, and the coloured regions show the 95%, 68%, and 50% confidence limits, as predicted by the posteriors of $\alpha = 0.6$, $\beta = 37$, and $\sigma_{QU} = 1.7$.

distribution of the relative position angle differences of B-field, intensity gradients, and local gravity, i.e. $\Delta\theta_{B,IG} = |(\theta_B - \theta_{IG})|$, $\Delta\theta_{B,LG} = |(\theta_B - \theta_{LG})|$, and $\Delta\theta_{IG,LG} = |(\theta_{IG} - \theta_{LG})|$. From the figure, it can be seen that the differences in the offset angles are mostly distributed towards the smaller angles. The median of $\Delta\theta_{B,IG}$, $\Delta\theta_{B,LG}$, and $\Delta\theta_{IG,LG}$ is 34° , 32° , and 30° with median absolute deviation of 22° , 18° , and 15° , respectively. The higher angular deviations in the histograms are primarily due to position angles in the elongated structures on the northeastern side, as well as from some structures located south of the CC.

As discussed previously, Koch et al. (2012a,b) developed a "polarization-intensity gradient method" that can estimate the local field-to-gravity force ratio Σ_B . This method is based on the assumption that the emission intensity gradients reflect the direction of matter flow due to the combined influences of magnetic pressure force and gravitational force. Using the MHD force equations and geometrically solving them by incorporating the angle between the magnetic field and intensity gradient ($\Delta_{B,IG}$), and between intensity gradient and local gravity ($\Delta_{IG,LG}$), the magnetic field (F_B)-to-gravity force (F_G) ratio can be obtained as

$$\Sigma_B = \frac{\sin(\Delta_{B,IG})}{\sin(90 - \Delta_{IG,LG})} = \frac{F_B}{|F_G|}. \quad (7)$$

In the above equation, the hydrostatic gas pressure is assumed to be negligible. Fig. 10 shows the Σ_B distribution plot over the Stokes $850 \mu\text{m}$ intensity map. From the figure, it can be seen that Σ_B is mostly ≤ 1 , with a median around ~ 0.6 , which shows that the magnetic field is not solely enough to balance the gravitational force (Koch et al. 2012a). This implies that gravity dominates over the magnetic field to govern the gas motion towards the centre. However, we note that the POL-2 images generally filter out large-scale structures, and so here, the intensity gradient only traces the local structure on a $4''$ pixel-scale. Therefore, to check the effect of large-scale structures on the intensity gradient and local gravity, we generated similar maps from *Herschel* $250 \mu\text{m}$ image of G148.24+00.41 and found that the maps are comparable with the JCMT maps. The use of $250 \mu\text{m}$ map is an optimal choice because compared to *Herschel's* longer wavelength (i.e. 350 and $500 \mu\text{m}$) bands, its resolution ($\sim 18''$) is comparable to the resolution of the JCMT $850 \mu\text{m}$ ($14''$) map and also it is a better

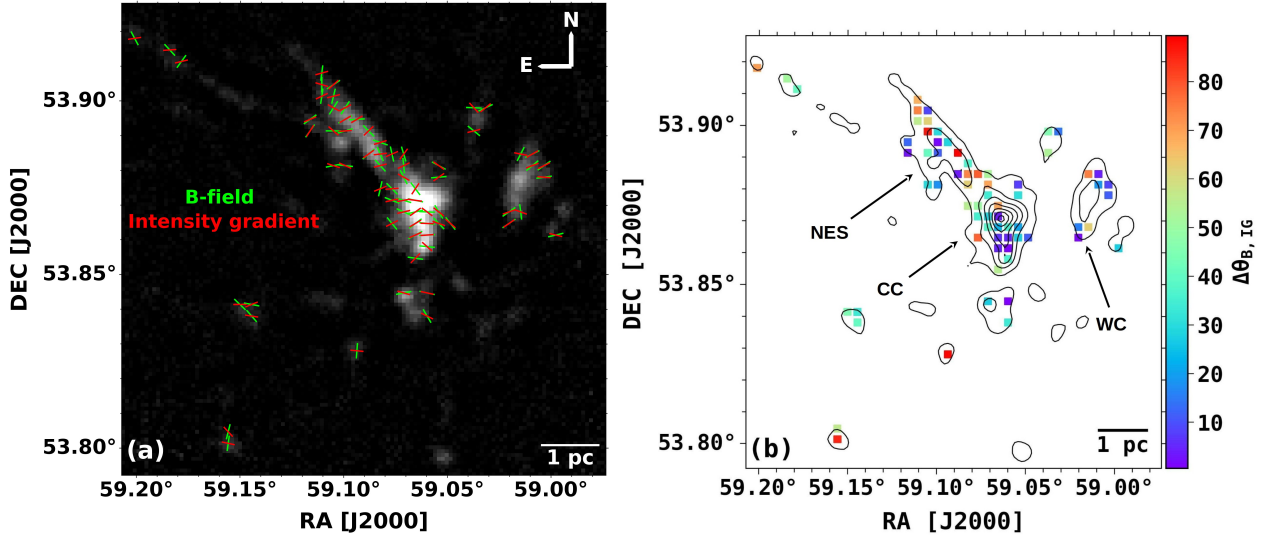


Figure 7. (a) The orientations of the B-fields (green segments) and intensity gradients (red segments) are overlaid on the 850 μm Stokes I map. (b) The distribution of the offset between the position angles of the B-fields and intensity gradients, i.e., $\Delta\theta_{B,IG} = |(\theta_B - \theta_{IG})|$ over the contours of 850 μm Stokes I map. The contour levels are same as in Fig. 2.

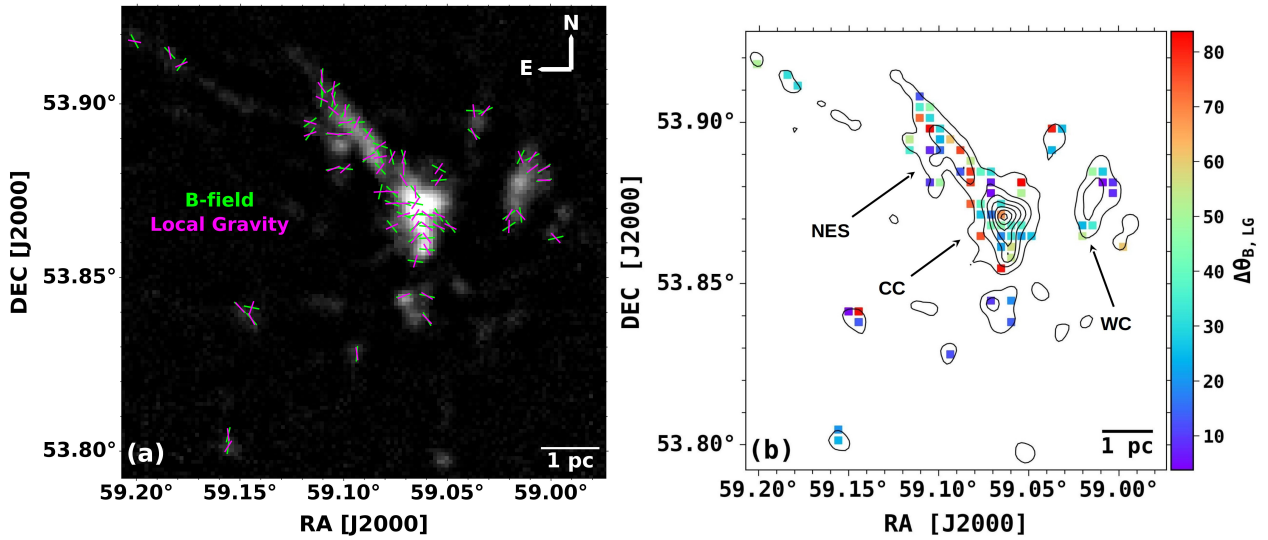


Figure 8. (a) The orientations of the B-fields (green segments) and local gravity (magenta vectors) are overlaid on the 850 μm Stokes I map. (b) The distribution of the offset between the position angles of the B-fields and local gravity, i.e., $\Delta\theta_{B,LG} = |(\theta_B - \theta_{LG})|$ over the 850 μm Stokes I map. The contour levels are same as in Fig. 2.

tracer of cold dust compared to *Herschel's* shorter wavelength (i.e. 70 and 160 μm) bands.

Due to the relatively low number of B-field segments in the WC region, we focused our further analysis, like the study of structure, dust properties, and B-field strength calculation, towards the CC and NES regions.

3.4 Column and number densities

We calculate the molecular hydrogen column density using the 850 μm dust continuum emission. Assuming the dust emission to be optically thin, the column density can be calculated using the relation (Kauffmann et al. 2008),

$$N(H_2) = 2.02 \times 10^{20} \text{cm}^{-2} \left(e^{1.439 \left(\frac{\lambda}{\text{mm}} \right)^{-1} \left(\frac{T_d}{10\text{K}} \right)^{-1}} - 1 \right) \times \left(\frac{\kappa_\nu}{0.01 \text{cm}^2 \text{g}^{-1}} \right)^{-1} \left(\frac{S_\nu}{\text{mJy beam}^{-1}} \right) \left(\frac{\theta_{\text{HPBW}}}{10''} \right)^{-2} \left(\frac{\lambda}{\text{mm}} \right)^3, \quad (8)$$

where S_ν is the flux density in Jy at frequency ν , λ is the wavelength (0.85 mm), T_d is the mean dust temperature in K, dust opacity $\kappa_\nu = 0.1(\nu/1 \text{ THz})^\beta = 0.0125 \text{ cm}^2 \text{g}^{-1}$ for $\nu = 0.353 \text{ THz}$ and dust opacity index, $\beta = 2$ (Battersby et al. 2011; Deharveng et al. 2012), and θ_{HPBW} is the beam size (14'' at 850 μm).

The mean T_d is taken from the *Herschel* Hi-GAL survey (Molinari et al. 2010) dust temperature map (Schisano et al. 2020) of the G148.24+00.41 region. Within the boundaries of CC and NES, the

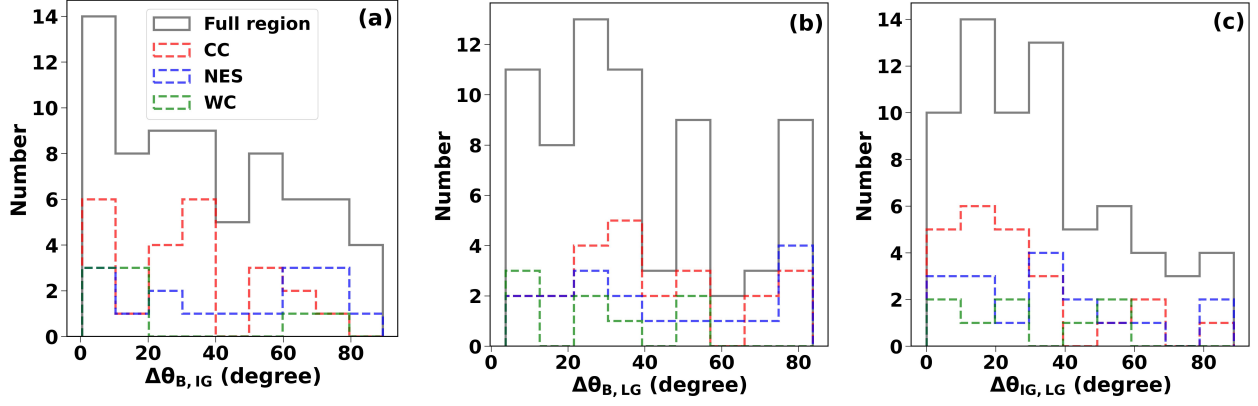


Figure 9. Distribution of difference in position angles of (a) magnetic field (θ_B) and intensity gradient (θ_{IG}), (b) magnetic field (θ_B) and local gravity (θ_{LG}), and (c) intensity gradient (θ_{IG}) and local gravity (θ_{LG}). The red, blue, and green histograms show the difference in position angles within the CC, NES, and WC regions, respectively.

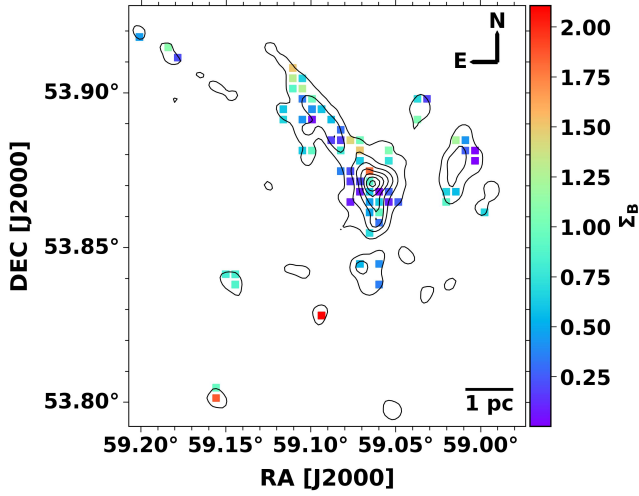


Figure 10. Σ_B distribution over the contours of 850 μm Stokes I map. The contour levels are same as in Fig. 2.

mean T_d is around ~ 16.8 K and 13.0 K, respectively. The total column density, $\sum N(H_2)$, for CC and NES, are found to be $(3.4 \pm 1.3) \times 10^{24} \text{ cm}^{-2}$ and $(1.9 \pm 0.7) \times 10^{24} \text{ cm}^{-2}$, respectively. Then, assuming the spherical geometry for CC, its number density (n_{H_2}) can be estimated using the relation

$$n_{H_2} = \frac{M}{V\mu m_H} = \frac{\sum N(H_2) \times A_{\text{pixel}}}{\frac{4}{3}\pi R_{\text{eff}}^3}, \quad (9)$$

where M and V are the mass and volume of the region, respectively, μ is the mean molecular weight assumed to be 2.8 (Kauffmann et al. 2008), m_H is the mass of hydrogen, A_{pixel} is the pixel area, and R_{eff} is the effective radius. The R_{eff} for CC is calculated as $(\text{Area}/\pi)^{0.5}$, and is around $\sim 0.9 \pm 0.1$ pc. Though NES is assumed as an elliptical structure with a semi-minor axis, $r_1 = 0.35 \pm 0.03$ pc and a semi-major axis, $r_2 = 1.10 \pm 0.09$ pc (see Fig. 2a), in 3-dimension, this elongated structure could be better described by a cylindrical geometry. Therefore, to calculate the number density of NES, we adopted its radius (r) and length (L) to be r_1 and $2r_2$, respectively. Under this approximation, we estimated the n_{H_2} for NES by using $V = \pi r^2 L$ in equation 9. The gas mass within the regions

is estimated from the total integrated molecular hydrogen column density, using equation 1 given in Rawat et al. (2023). The total column density, n_{H_2} , and the mass of the regions are given in Table 1. The uncertainties in the estimated cloud parameters are mainly due to uncertainty in the gas-to-dust ratio (23%), the dust opacity index (30%), and the distance of the cloud (9%) (Rawat et al. 2023, and references therein).

3.5 Velocity dispersion

We used $C^{18}O$ molecular line data to determine the non-thermal velocity dispersion along the line-of-sight. Rawat et al. (2024) found that in comparison to ^{12}CO and ^{13}CO , $C^{18}O$ emission is optically thin in the G148.24+00.41 cloud. Fig. 11 shows the $C^{18}O$ spectra averaged within the boundary of the two regions, CC and NES. The Gaussian fitting over the spectra gives the mean velocity as $-34.15 \pm 0.04 \text{ km s}^{-1}$ and $-33.80 \pm 0.04 \text{ km s}^{-1}$, and velocity dispersion (σ_{obs}) as $0.69 \pm 0.05 \text{ km s}^{-1}$ and $0.41 \pm 0.03 \text{ km s}^{-1}$, for CC and NES, respectively.

The non-thermal velocity dispersion (σ_{nt}) can be calculated using the relation, $\sigma_{\text{nt}} = \sqrt{\sigma_{\text{obs}}^2 - \sigma_{\text{th}}^2}$, where σ_{th} is the thermal velocity dispersion, defined as $\sqrt{\frac{K_B T_k}{M_{C^{18}O}}}$. Here, K_B is the Boltzmann constant, T_k is the gas kinetic temperature, and $M_{C^{18}O}$ is the mass of $C^{18}O$ molecule (30 amu). We have used the excitation temperature map from Rawat et al. (2024) to get the approximate values of T_k , as 11.4 K and 10.3 K for CC and NES, respectively. The estimated σ_{th} for the regions is $\sim 0.06 \text{ km s}^{-1}$ and 0.05 km s^{-1} , respectively, and hence negligible, leading $\sigma_{\text{nt}} \sim \sigma_{\text{obs}}$. This is an indication of the presence of turbulence in CC and NES, which has also been reported in Rawat et al. (2024) for the C1 clump.

3.6 Magnetic field strength

Davis (1951) and Chandrasekhar & Fermi (1953) proposed a method to estimate the plane-of-sky component of the magnetic field (B_{pos}), known as the Davis-Chandrasekhar-Fermi (DCF) method, which is based on the assumption that the turbulence-induced Alfvén waves perturb the ordered B-field structure. Therefore, there will be a distorted component of the B-field that would appear as an irregular

Table 1. Parameters estimated for CC and NES.

No	Parameter	Unit	CC	NES
1	Effective radius (R_{eff})	pc	0.9 ± 0.1	semi-minor axis (r_1) = 0.35 ± 0.03 , semi-major axis (r_2) = 1.10 ± 0.09
2	Mean column density ($N(H_2)$)	cm^{-2}	$(5.8 \pm 2.2) \times 10^{21}$	$(7.1 \pm 2.7) \times 10^{21}$
3	Number density (n_{H_2})	cm^{-3}	1560 ± 780	3290 ± 1645
4	Mass (M)	M_\odot	330 ± 148	188 ± 85
5	Mean dust temperature (T_d)	K	16.8	13.0
6	Observed velocity dispersion (σ_{obs})	km s^{-1}	0.69 ± 0.05	0.41 ± 0.03
7	Thermal velocity dispersion (σ_{th})	km s^{-1}	0.06	0.05
8	Non-thermal velocity dispersion (σ_{nt})	km s^{-1}	0.69 ± 0.05	0.41 ± 0.03
Structure function analysis				
1	Turbulent-to-ordered magnetic field energy ratio $\left(\frac{\langle \delta B^2 \rangle^{1/2}}{B_0}\right)$		0.43 ± 0.01	0.46 ± 0.04
2	Angular dispersion (σ_θ)	degrees	22.7 ± 0.6	23.9 ± 1.5
3	Plane-of-sky magnetic field strength (B_{pos})	μG	24.0 ± 6.0	20.0 ± 5.0
4	Mass-to-flux ratio (Λ_B)		1.8 ± 0.8	2.7 ± 1.2
5	Alfvén velocity (V_A)	km s^{-1}	1.0 ± 0.4	0.6 ± 0.2
6	Alfvén mach number (M_A)		1.2 ± 0.4	1.2 ± 0.4
7	Magnetic pressure (P_B)	dyne cm^{-2}	$(3.7 \pm 1.9) \times 10^{-11}$	$(2.6 \pm 1.3) \times 10^{-11}$
8	Turbulent pressure (P_{turb})	dyne cm^{-2}	$(5.2 \pm 2.7) \times 10^{-11}$	$(2.5 \pm 1.3) \times 10^{-11}$
Virial balance				
1	Kinetic energy (E_K)	J	$(4.7 \pm 2.2) \times 10^{38}$	$(6.3 \pm 3.0) \times 10^{37}$
2	Magnetic energy (E_B)	J	$(3.3 \pm 3.0) \times 10^{38}$	$(7.0 \pm 5.0) \times 10^{37}$
3	Gravitational energy (E_G)	J	$(10.4 \pm 9.0) \times 10^{38}$	$(14 \pm 12) \times 10^{37}$
4	Kinetic virial parameter ($\alpha_{vir,k}$)		0.9 ± 0.4	0.9 ± 0.4
5	Total virial parameter ($\alpha_{vir,tot}$)		1.2 ± 0.6	1.4 ± 0.7

scatter in polarization angles in comparison to those that are produced by large-scale ordered B-field. Thus, the DCF method implies that the ratio of turbulent (δB) to ordered B-field (B_0) is proportional to the ratio of non-thermal velocity dispersion (σ_{nt}) to Alfvén velocity ($V_A = B_0/\sqrt{4\pi\rho}$, ρ is the gas mass density), i.e. $\frac{\delta B}{B_0} = \frac{\sigma_{nt}}{V_A}$. Also, the dispersion in the B-field position angles (σ_θ) about the large-scale ordered B-field is assumed as $\sigma_\theta = \frac{\delta B}{B_0}$. Using these relations, the plane-of-sky magnetic field component, B_{pos} can be estimated as

$$B_{pos} = Q\sqrt{4\pi\rho} \frac{\sigma_{nt}}{\sigma_\theta}, \quad (10)$$

where Q is the correction factor for the line-of-sight and beam-integration effects (Ostriker et al. 2001). The studies show that the beam-integration effect can lead to an underestimation of angular dispersion in polarization angles, resulting in an overestimation of the magnetic field strength (Ostriker et al. 2001; Padoan et al. 2001; Houde et al. 2009). To determine the angular dispersion, there are different statistical methods (see Hildebrand et al. 2009; Houde et al. 2009; Pattle et al. 2017; Liu et al. 2022), which are used in the literature. In this work, we use the structure-function (SF; Hildebrand et al. 2009) method, which gives

the $\frac{\delta B}{B_0}$ ratio by accounting for the spatial variation of position angles.

3.6.1 Structure function analysis

In the SF method, the magnetic field is assumed to be composed of a large-scale structured field and a turbulent field that are statistically independent. The distinctive behaviour of the two components enables them to distinguish and extract the turbulent component, facilitating the computation of σ_θ . The SF method computes the difference in position angles, $\Delta\phi(l) \equiv \phi(\mathbf{x}) - \phi(\mathbf{x} + \mathbf{l})$, between the $N(l)$ pairs of pixels separated by $l = |\mathbf{l}|$, using the following function:

$$\langle \Delta\phi^2(l) \rangle^{1/2} \equiv \left(\frac{1}{N(l)} \sum_{i=1}^{N(l)} [\phi(\mathbf{x}) - \phi(\mathbf{x} + \mathbf{l})]^2 \right)^{1/2}. \quad (11)$$

This function is referred to as the "angular dispersion function". We want to point out that the polarization position angles are used here for the dispersion function. The angular dispersions, $\Delta\phi$, are kept $\leq 90^\circ$, to avoid the effect of the $\pm 180^\circ$ ambiguity of the magnetic field lines. Under the limit, $\delta < l \ll d$, the square of the angular dispersion function, known as the "structure function" is characterised by (Hildebrand et al. 2009)

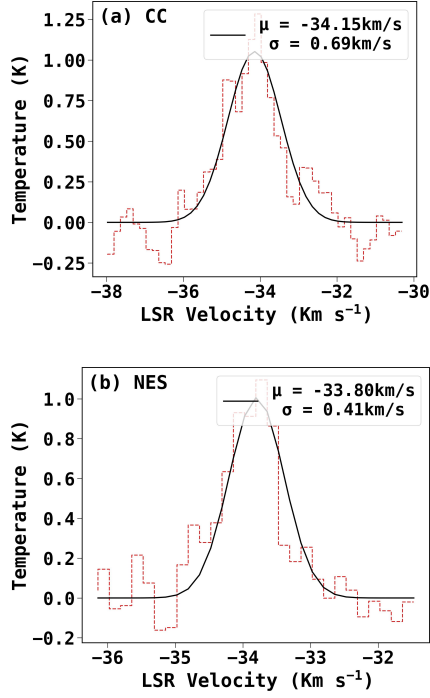


Figure 11. $C^{18}O$ average spectral profile for (a) CC (central clump) and (b) NES (northeastern elongated structure).

$$\langle \Delta\phi^2(l) \rangle_{tot} - \sigma_M^2(l) \simeq b^2 + m^2 l^2, \quad (12)$$

where δ is the correlation length of the turbulent component, and d is the typical length for variation in large-scale B-field. The quadratically added terms in the dispersion function, $m^2 l^2$ and b^2 , are the contribution from the B_0 and δB , respectively. The B_0 is expected to increase almost linearly with slope m for $l \ll d$, and b is a constant turbulent contribution for $l > \delta$ (for details, see Hildebrand et al. 2009). The $\sigma_M^2(l)$ is the contribution from the measured uncertainty in the position angles.

The turbulent to large-scale magnetic field strength is given by (Hildebrand et al. 2009)

$$\frac{\langle \delta B^2 \rangle^{1/2}}{B_0} = \frac{b}{\sqrt{2 - b^2}}, \quad (13)$$

and B_0 can be estimated by using the modified DCF relation:

$$B_0 \simeq \sqrt{(2 - b^2) 4\pi \mu m_H n_{H_2} \frac{\sigma_{nt}}{b}}. \quad (14)$$

Using the Q correction factor, we can determine the plane-of-sky magnetic field strength:

$$B_{pos} = QB_0, \quad (15)$$

where Q is taken to be 0.5 (Heitsch et al. 2001; Ostriker et al. 2001).

We calculated the dispersion function corrected by measurement uncertainty, i.e. $\langle \Delta\phi^2(l) \rangle_{tot} - \sigma_M^2(l)$ with a bin size of $12''$. We used various bin sizes and found that the fit is converged, and fitting

errors are the least for $12''$. Fig. 12 shows the dispersion in position angles as a function of the length scale for CC and NES. We fitted the dispersion function with the model defined in equation 12 using least square fit, over the first few data points to ensure the limit, $l \ll d$. The best-fits turbulent component, b , for CC and NES are $32^\circ.1 \pm 0^\circ.9$ and $33^\circ.8 \pm 2^\circ.1$, respectively. The dispersion in position angles can be obtained as $\sigma_\theta = b/\sqrt{2}$, which is around $\sim 22^\circ.7 \pm 0^\circ.6$ and $23^\circ.9 \pm 1^\circ.5$ for CC and NES, respectively. These values are close to the maximum value at which the DCF methods would give reliable results ($\sigma_\theta \leq 25^\circ$, Ostriker et al. 2001) if a correction factor of 0.5 is applied. Using equation 13, 14, and 15, we calculate the $\frac{\delta B}{B_0}$ ratio to be around $\sim 0.43 \pm 0.01$ and 0.46 ± 0.04 , and B_{pos} to be around $\sim 24.0 \pm 6.0 \mu\text{G}$ and $20.0 \pm 5.0 \mu\text{G}$, for CC and NES, respectively. All the estimated parameters are given in Table 1.

4 DISCUSSION

The plane-of-sky magnetic field strength for the CC and NES regions is around $\sim 24 \mu\text{G}$ and $20 \mu\text{G}$, respectively. Given the uncertainty of at least a factor of 2 associated with the B-field estimation by the DCF method (Crutcher 2012), the estimated B-field strengths are within the range of ~ 10 – $100 \mu\text{G}$ observed in star-forming regions (Chapman et al. 2011; Crutcher 2012; Pattle et al. 2022). The values are also consistent (i.e. within a factor of 1.5) with the upper limits of the B-field values from Crutcher et al. (2010) relation for the respective density of the regions.

4.1 Correlation between magnetic fields, intensity gradients, and local gravity

Due to the low statistics in the polarization data, it is difficult to conclusively comment on the overall morphology of the B-field, intensity gradients, and local gravity. However, through this comparison, some inferences can be drawn over their relative spatial variance. Fig. 7 and 8 shows a correlation between the B-field, intensity gradients, and local gravity in the CC and WC regions, whereas the differences in their position angles are relatively higher in the NES region. This correlation can be due to the collapse of the clumps where gravity has pulled in and aligned B-field lines with the intensity gradients, in the CC and WC regions (Koch et al. 2013; Wang et al. 2019). However, in the outer diffused regions, like the elongated structures, the field lines are not yet that much affected by the local gravity.

Some simulations of the global collapse of magnetized clouds have found that the gravitational flows from large scale to small scale, i.e. from filaments to clumps/cores, can drag the magnetic field lines along the flow, causing a “U” shaped geometry of the field lines across the filament spine (Gómez et al. 2018; Vázquez-Semadeni et al. 2019). We also found evidence of “U” shaped geometry of B-field lines, at the bottom of the elongated part of the central clump. Fig. 13 shows the zoomed-in view of the central clump region, in which the “U” shaped geometry is sketched from the observed B-field orientations and is shown by magenta curves. High-resolution and sensitivity observations would be required to ascertain the observed morphology. A similar effect of gravity over the B-field morphology has also been found in other observational works (Tang et al. 2019; Wang et al. 2020a,b; Beuther et al. 2020; Busquet 2020; Pillai et al. 2020).

In G148.24+00.41, Rawat et al. (2024), using MWISP CO data,

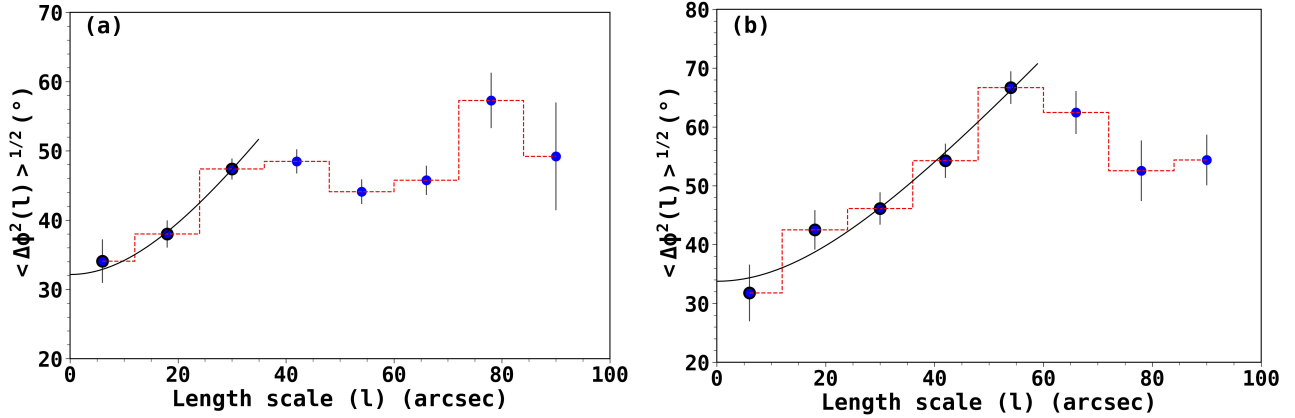


Figure 12. The angular dispersion function for (a) CC and (b) NES. The solid curve represents the best-fit model to the data, and the points used for fitting are shown in black encircled circles. The intercept of the best-fit model ($l = 0$) gives the turbulent contribution to the total angular dispersion. The error bars denote the statistical uncertainties after binning and propagating the individual measurement uncertainties.

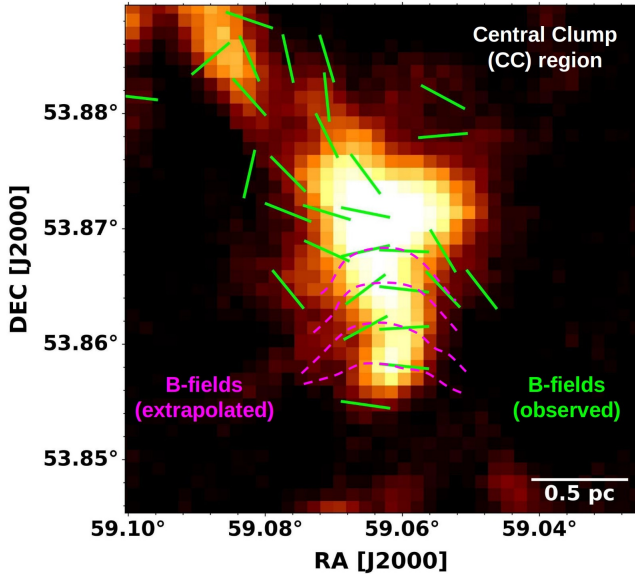


Figure 13. Stokes I map of the Central clump region of G148.24+00.41, over which the observed B-field segments are shown (green segments). The B-field segments show a “U” shaped geometry, sketched with observed segments and shown by magenta dashed curves, which may be caused by the drag of gravitational converging flows towards the centre of the cloud.

identified filamentary gas flows exhibiting noticeable velocity gradients as they move towards the hub. They found that the velocity gradient increases towards the hub, with a measured value of $\sim 0.2 \text{ km s}^{-1} \text{ pc}^{-1}$ in the proximity of the hub. The aforementioned findings give evidence of accreting gas flows along the filaments towards the cloud’s centre, which can affect the B-field morphology by dragging them along the flow. Future high-resolution dust continuum and polarimetric observations might be able to reveal a significant number of polarization vectors at the clump/core scale to better resolve the substructures and the B-field morphology around the hub of G148.24+00.41.

4.2 Gravitational stability

4.2.1 Mass-to-flux ratio

In order to investigate whether the magnetic field can provide stability to the regions against gravitational collapse, we determine the mass-to-flux ratio (Crutcher et al. 2004). It is generally calculated as a dimensionless critical stability parameter, λ_B , which is basically the comparison of the mass to magnetic flux ratio with the critical ratio (Crutcher et al. 2004):

$$\lambda_B = \frac{(M/\phi)_{obs}}{(M/\phi)_{crit}} = 7.6 \times 10^{-21} \frac{N(H_2)(\text{cm}^{-2})}{B_{pos}(\mu\text{G})}, \quad (16)$$

where $N(H_2)$ is the mean column density of the region. A clump or dense core is magnetically supercritical ($\lambda_B > 1$) if the magnetic field is not strong enough to support the system against gravitational collapse, whereas a strong magnetic field would make the system magnetically subcritical ($\lambda_B < 1$), i.e. stable against collapse. Using the mean $N(H_2) \sim (5.8 \pm 2.2) \times 10^{21} \text{ cm}^{-2}$ and $(7.1 \pm 2.7) \times 10^{21} \text{ cm}^{-2}$, we calculated the critical parameter to be around $\sim 1.8 \pm 0.8$ and 2.7 ± 1.2 for CC and NES, respectively. The critical parameter shows that both regions are magnetically supercritical. In general, a statistical correction factor is applied to λ_B to account for bias due to geometric effects (Crutcher et al. 2004). Different correction factors are suggested for different geometry of clumps with respect to magnetic field, e.g., $\pi/4$ for spherical clump and $1/3$ for oblate spheroid with major-axis perpendicular to the mean B-field (Crutcher et al. 2004), and $3/4$ for prolate spheroid with major-axis parallel to the mean B-field (Planck Collaboration et al. 2016). Using these correction factors, the mass-to-flux ratios become subcritical to transcritical/supercritical in the range of 0.6 to 1.4 for CC with mean ~ 1.1 , and 0.9 to 2.1 for NES with mean ~ 1.7 . However, if we consider the overestimation of B_{pos} in the DCF method itself, our estimated mass-to-flux ratios could also be a lower limit. We want to acknowledge here that the estimated B-field strengths and mass-to-flux ratios are only averaged values over the selected regions. The regions can still be super-critical inside but sub-critical in the outer part, as also shown in a recent simulation by Gómez et al. (2021).

4.2.2 Turbulence versus magnetic field

Simulations suggest that turbulence plays a dual role in the clouds and their substructures by providing turbulent support against the gravitational collapse at a large scale while producing compressions and shocks at small scales, that create density enhancements and trigger the star formation process (Mac Low & Klessen 2004; Ballesteros-Paredes et al. 2007; Hennebelle & Falgarone 2012; Klessen & Glover 2016). Also, whether it is turbulence (weak B-field models) or magnetic field (strong B-field models) or both, is a subject of investigation regarding their respective roles in the formation of clumps, cores, and subsequent star formation within these structures. In order to investigate their impact, we need to find out the relative strength of turbulence in comparison to the magnetic field.

The Alfvén Mach number (M_A) infers the relative importance of turbulence and magnetic field in molecular clouds and is defined as $M_A = \sqrt{3}\sigma_{nt}/V_A$. The Alfvén velocity is calculated as, $V_A = B_{tot}/\sqrt{4\pi\rho}$. The total B-field strength (B_{tot}) of the regions can be determined by using a statistical relation, $B_{tot} = (4/\pi)B_{pos}$ (Crutcher et al. 2004). For CC and NES, the B_{tot} is found to be around $31 \pm 8 \mu\text{G}$ and $26 \pm 6 \mu\text{G}$, respectively. Using the mass density estimated within the dimensions of two regions (given in Table 1) and corresponding B_{tot} values, the V_A for CC and NES are found to be $\sim 1.0 \pm 0.4 \text{ km s}^{-1}$ and $0.6 \pm 0.2 \text{ km s}^{-1}$, respectively. Then, using the corresponding σ_{nt} values, the M_A is calculated to be around $\sim 1.2 \pm 0.4$ for both the two regions. A star-forming region is super-Alfvénic if $M_A > 1$, which means that the turbulent pressure is higher than the magnetic pressure. Conversely, it will be sub-Alfvénic if $M_A < 1$, which means that the magnetic pressure is higher than the turbulent pressure. In the present case, both the regions are trans Alfvénic.

We also calculated the magnetic and turbulent pressures using the relations:

$$P_B = \frac{B_{tot}^2}{8\pi} \quad \text{and} \quad P_t = \frac{3}{2}\rho\sigma_{nt}^2 \quad (\text{Spherical}), \quad (17)$$

$$= \rho\sigma_{nt}^2 \quad (\text{Cylindrical}),$$

here, a factor of 3/2 is included to estimate the total turbulent pressure by assuming the non-thermal velocity dispersion to be isotropic in spherical geometry. For the CC region, the magnetic and turbulent pressure is found to be $\sim (3.7 \pm 1.9) \times 10^{-11} \text{ dyne cm}^{-2}$ and $\sim (5.2 \pm 2.7) \times 10^{-11} \text{ dyne cm}^{-2}$, respectively. For the NES region, P_B and P_t are $\sim (2.6 \pm 1.3) \times 10^{-11} \text{ dyne cm}^{-2}$ and $(2.5 \pm 1.3) \times 10^{-11} \text{ dyne cm}^{-2}$, respectively. In the CC region, the turbulent pressure is higher than the magnetic pressure by a factor of ~ 1.4 , while in NES, the pressure values are similar. Also, the thermal pressure ($\sim \rho\sigma_{th}^2$) in both regions, is much smaller than the turbulent and magnetic pressure, which shows that the thermal energy plays a negligible role in energy balance. So, from the Alfvén Mach number and pressure estimation, it seems that the turbulence is slightly more dominant in comparison to the magnetic field in CC, i.e. in the centremost part of G148.24+00.41, while it is similar in the NES.

4.2.3 Virial analysis

The virial theorem is a principle that relates the average kinetic energy (E_K) and magnetic field energy (E_B) of a system to its average gravitational potential energy (E_G), which provides insights into the

stability and energy distribution of the system. The Virial theorem is written as:

$$\frac{1}{2} \frac{d^2 I}{dt^2} = 2E_K + E_B + E_G, \quad (18)$$

where I is the moment of inertia. The surface energy terms here are neglected. The kinetic energy term is given by (Fiege & Pudritz 2000)

$$E_K^{sph} = \frac{3}{2} M \sigma_{obs}^2 \quad (\text{Spherical}), \quad (19)$$

$$E_K^{cyl} = M \sigma_{obs}^2 \quad (\text{Cylindrical}),$$

where M is the mass and $\sigma_{obs}^2 = \sigma_{th}^2 + \sigma_{nt}^2$. The magnetic field energy is given by

$$E_B = \frac{1}{2} M V_A^2 \quad (20)$$

and the gravitational potential energy is given by

$$E_G^{sph} = -\frac{(3-a)}{(5-2a)} \frac{GM^2}{R} \quad (\text{Spherical}), \quad (21)$$

$$E_G^{cyl} = -\frac{GM^2}{L} \quad (\text{Cylindrical}),$$

where G is the gravitational constant, R , is the effective radius of the sphere, and L is the length of the cylinder. Here a is the density profile index of the sphere ($\rho \propto r^{-a}$). The energy values for the two regions are listed in Table 1. We found that for CC, $|E_G| > E_K > E_B$ (i.e. 10.4:4.7:3.3), while for NES, $|E_G| > E_K \approx E_B$ (i.e. 14:6.3:7.0), which restates the results of Alfvén Mach number and mass-to-flux ratio calculation, i.e. turbulence is slightly more dominant than the magnetic field in CC, while it is similar in NES, but overall the gravity is the dominant factor in both the regions. Nevertheless, the calculation of individual energy terms is an important exercise, enabling the direct comparison of various forces that govern the evolution of clumps/structures, expressed in the same units.

For a non-magnetized system ($E_B = 0$), the stability criteria is given by $2E_K + E_G < 0$, and based on this condition, the kinetic virial parameter is defined as (Bertoldi & McKee 1992)

$$\alpha_{vir,k} = \frac{2E_K}{|E_G|} = \frac{3(5-2a)}{(3-a)} \frac{R\sigma_{obs}^2}{GM} \quad (\text{Spherical}), \quad (22)$$

$$= \frac{2L}{GM} \sigma_{obs}^2 \quad (\text{Cylindrical}).$$

Using the M , R , L , and σ_{obs} values of the regions (given in Table 1) in equation 22, and adopting $a = 2$ for spherical case, we calculate the $\alpha_{vir,k}$ to be around 0.9 ± 0.4 and 0.9 ± 0.4 , respectively for CC and NES. The derived $\alpha_{vir,k} < 2$ means that in the case of a non-magnetized sphere ($E_B = 0$), the thermal plus turbulent contribution is not enough to provide stability to the regions against the gravitational collapse (Kauffmann et al. 2013; Mao et al. 2020). Including the magnetic energy term in the stability criteria, i.e. $2E_K + E_B + E_G < 0$, the total virial parameter is calculated using the modified relation (Bertoldi & McKee 1992; Pillai et al. 2011; Sanhueza et al. 2017).

$$\alpha_{vir,tot} = \frac{2E_K + E_B}{|E_G|} = \frac{3(5-2a)}{(3-a)} \frac{R}{GM} \left(\sigma_{obs}^2 + \frac{V_A^2}{6} \right) \quad (\text{Spherical}), \quad (23)$$

$$= \frac{2L}{GM} \left(\sigma_{obs}^2 + \frac{V_A^2}{4} \right) \quad (\text{Cylindrical}).$$

With the magnetic support, the $\alpha_{vir,tot}$ value is estimated to be around $\sim 1.2 \pm 0.6$ and 1.4 ± 0.7 for CC and NES, respectively. The $\alpha_{vir,tot}$ values for the regions are < 2 , which shows that the two regions are bound by gravity and thus can collapse to form stars. The virial analysis shows that the total kinetic energy (E_K , i.e. thermal plus turbulent) in both regions is not sufficient to support them against the gravitational collapse. While magnetic energy, combined with kinetic energy, is found to be comparable to gravitational potential energy.

In the present work, we have estimated magnetic field strengths and derived various parameters for the CC and NES regions. However, we want to stress that these results must be taken with caution as the measurements are uncertain within a factor two due to the inherent large uncertainty in the mass and density of the studied regions. Moreover, the modified DCF methods can be uncertain up to a factor of two or more (Crutcher 2012), and also, the B-field strength in the studied regions can be biased due to the limited number of B-field segments traced by our observations. Due to all these uncertainties, the mass-to-flux ratio and virial status of the regions should be considered as qualitative indicators of the stability of the region. In the present case, we have used the generally accepted Q value of 0.5 (Crutcher 2012) in our estimations, however, if we use $Q = 0.4$, suggested for parsec scale clumps (Padoan et al. 2001), similar to our studied regions, the B-field strengths will reduce by a factor of ~ 1.2 . As a consequence, the CC and NES regions would become more magnetically supercritical. Future high-resolution and more sensitive observations would better constrain the magnetic field and turbulence properties of the hub. However, taking the measured mass-to-flux ratio and virial parameters at face value, it can be argued that, at present, gravity has overall an upper hand over magnetic and kinetic energies in CC and NES, which is consistent with the formation of a young cluster noticed by Rawat et al. (2023) in the hub.

4.3 The criticality of magnetic fields in hub-filamentary clumps

Like the CC of G148.24+00.41, the clumps located at the junction of the hub-filamentary systems are known to be potential sites of cluster formation (e.g. Kumar et al. 2020), because such clumps are attached to converging filamentary structures that fuel them with cold gaseous matter (e.g. Myers 2009; Li et al. 2014; Treviño-Morales et al. 2019; Kumar et al. 2022). Although physical processes that govern the star formation are scale-dependent, it is worthwhile to compare the global properties of the parsec or sub-parsec scale hub filamentary clumps studied with similar resolution. In the literature, a few such clumps have been studied with JCMT/POL2, these are: IC 5146 E-hub (Wang et al. 2019), G33.92+0.11 (Wang et al. 2020b), Mon R2 (Hwang et al. 2022), IC 5146 W-hub (Chung et al. 2022), and SDC13 (Wang et al. 2022). In the majority of these hub filamentary clumps, except Mon R2, the mass-to-flux ratio and/or virial analysis suggest the dominance or edge of gravitational energy over the magnetic and

kinetic energies, similar to the CC region of G148.24+00.41. We found that all the aforementioned clumps are associated with either protostars or an embedded cluster (e.g. Harvey et al. 2008; Gutermuth et al. 2009; Peretto et al. 2014; Liu et al. 2015). Thus, it seems that, at least for those parsec scale hubs that are in the early stages of cluster formation, like the CC of G148.24+00.41, gravity has an upper hand on the energy budget of the system. A large sample of hub-filamentary clumps of various evolutionary stages (e.g. from pre-stellar clumps to clumps hosting emerging clusters of different ages) would be valuable to study the time evolution of various physical processes that govern star formation and its evolution.

5 SUMMARY

We have performed the dust polarization observation of the central part of the G148.24+00.41 cloud to investigate the B-field morphology and its strength relative to gravity and turbulence, using JCMT SCUBA-2/POL-2 at 850 μm . We specifically focused on the C1 clump, located at the hub of G148.24+00.41. The main results are summarised below:

- The 850 μm Stokes I intensity map reveals the presence of a central clump (CC), northeastern elongated structure (NES), and western clump (WC) around the hub of G148.24+00.41. The B-field segments of CC and NES regions show mixed morphology, while the WC region shows converging B-field segments, mostly aligned along the southeast direction.
- We found evidence of the depolarization effect, and from the Bayesian analysis over the non-debiased polarization data, found a power-law index, $\alpha = 0.6$. Although this shows a decreasing level of dust grain alignment, but they can still be aligned with the magnetic field in the central high-density region of the cloud.
- We compared the relative orientations of B-fields (θ_B), intensity gradients (θ_{IG}), and local gravity (θ_{LG}) over the full map. In the CC and WC regions, the three factors are mostly correlated, while the difference in orientations is higher in the NES region. This suggests that gravity is dragging the intensity gradients and aligning them with the B-fields in the CC and WC clump, while the effect of gravity in NES is comparatively less significant.
- We constructed the Σ_B map to see the localised B-field strength in comparison to local gravity, and found that for most of the parts, $\Sigma_B < 1$, i.e. gravitational force is dominant over the magnetic field force.
- We used the structure function analysis to determine the B-field strength, and as a result, found B_{pos} for CC and NES to be around $\sim 24.0 \pm 6.0 \mu\text{G}$ and $20.0 \pm 5.0 \mu\text{G}$, respectively. In both regions, the turbulent component relative to the organised magnetic field structure was determined to be approximately 0.4–0.5.
- The mass-to-flux ratio and Alfvén Mach number calculation for CC and NES shows that both regions are magnetically trans-critical/supercritical and trans-Alfvénic. The turbulent pressure was found to be higher than the magnetic pressure in CC, while they are similar in NES.
- The virial analysis shows that for CC, the $|E_G| > E_K > E_B$ (i.e. 10.4:4.7:3.3), while for NES, $|E_G| > E_K \approx E_B$ (i.e. 14:6.3:7.0). The magnetic field and turbulence individually are not strong enough to provide stability to the regions against gravity. Both regions were found to be bound by gravity.

Overall, we find that currently, gravitational energy has an edge over the other energy terms of the hub region of G148.24+00.41, thereby continue to facilitate the growth of the young cluster in the

hub, although we acknowledge that given the large uncertainties associated with our estimates, a conclusive answer would require further precise measurements of magnetic field and cloud properties.

ACKNOWLEDGEMENT

We thank the anonymous referee for the comments and suggestions that helped to improve the paper. The research work at the Physical Research Laboratory is funded by the Department of Space, Government of India. CE acknowledges the financial support from grant RJF/2020/000071 as a part of the Ramanujan Fellowship awarded by the Science and Engineering Research Board (SERB), Department of Science and Technology (DST), Government of India. The James Clerk Maxwell Telescope is operated by the East Asian Observatory on behalf of The National Astronomical Observatory of Japan; Academia Sinica Institute of Astronomy and Astrophysics; the Korea Astronomy and Space Science Institute; the National Astronomical Research Institute of Thailand; Center for Astronomical Mega-Science (as well as the National Key R&D Program of China with No. 2017YFA0402700). Additional funding support is provided by the Science and Technology Facilities Council of the United Kingdom and participating universities and organizations in the United Kingdom, Canada, and Ireland. The authors wish to recognize and acknowledge the very significant cultural role and reverence that the summit of Maunakea has always had within the indigenous Hawaiian community. The data taken in this paper was observed under the project code M22BP055. D.K.O. acknowledges the support of the Department of Atomic Energy, Government of India, under project identification No. RTI 4002. We thank Junhao Liu for the discussion on the DCF methods. This research made use of the data from the Milky Way Imaging Scroll Painting (MWISP) project, which is a northern galactic plane CO survey with the PMO-13.7m telescope. We are grateful to all the members of the MWISP working group, particularly the staff members at PMO-13.7m telescope, for their long-term support. MWISP was sponsored by the National Key R&D Program of China with grant 2017YFA0402701 and CAS Key Research Program of Frontier Sciences with grant QYZDJ-SSW-SLH047.

Facilities: JCMT, PMO

DATA AVAILABILITY

The JCMT data used in this work can be shared on reasonable request. We also used the CO molecular data from PMO, which can be shared by the PMO database on reasonable request to the project team.

REFERENCES

- Andersson B. G., Lazarian A., Vaillancourt J. E., 2015, *ARA&A*, **53**, 501
- André P., Könyves V., Arzoumanian D., Palmeirim P., Peretto N., 2013, in Kawabe R., Kuno N., Yamamoto S., eds, *Astronomical Society of the Pacific Conference Series Vol. 476, New Trends in Radio Astronomy in the ALMA Era: The 30th Anniversary of Nobeyama Radio Observatory*. p. 95
- Ballesteros-Paredes J., Klessen R. S., Mac Low M. M., Vázquez-Semadeni E., 2007, in Reipurth B., Jewitt D., Keil K., eds, *Protostars and Planets V*. p. 63 ([arXiv:astro-ph/0603357](https://arxiv.org/abs/astro-ph/0603357)), doi:10.48550/arXiv.astro-ph/0603357
- Battersby C., et al., 2011, *A&A*, **535**, A128
- Bertoldi F., McKee C. F., 1992, *ApJ*, **395**, 140
- Beuther H., Vlemmings W. H. T., Rao R., van der Tak F. F. S., 2010, *ApJ*, **724**, L113
- Beuther H., et al., 2018, *A&A*, **614**, A64
- Beuther H., et al., 2020, *The Astrophysical Journal*, **904**, 168
- Busquet G., 2020, *Nature Astronomy*, **4**, 1126
- Chandrasekhar S., Fermi E., 1953, *ApJ*, **118**, 113
- Chapin E. L., Berry D. S., Gibb A. G., Jenness T., Scott D., Tilanus R. P. J., Economou F., Holland W. S., 2013, *MNRAS*, **430**, 2545
- Chapman N. L., Goldsmith P. F., Pineda J. L., Clemens D. P., Li D., Krčo M., 2011, *ApJ*, **741**, 21
- Chung E. J., Lee C. W., Kwon W., Yoo H., Soam A., Cho J., 2022, *AJ*, **164**, 175
- Chung E. J., Lee C. W., Kwon W., Tafalla M., Kim S., Soam A., Cho J., 2023, *The Astrophysical Journal*, **951**, 68
- Cox N. L. J., et al., 2016, *A&A*, **590**, A110
- Crutcher R. M., 2012, *ARA&A*, **50**, 29
- Crutcher R. M., Nutter D. J., Ward-Thompson D., Kirk J. M., 2004, *ApJ*, **600**, 279
- Crutcher R. M., Wandelt B., Heiles C., Falgarone E., Troland T. H., 2010, *ApJ*, **725**, 466
- Currie M. J., Berry D. S., Jenness T., Gibb A. G., Bell G. S., Draper P. W., 2014, in Manset N., Forshay P., eds, *Astronomical Society of the Pacific Conference Series Vol. 485, Astronomical Data Analysis Software and Systems XXIII*. p. 391
- Davis L., 1951, *Physical Review*, **81**, 890
- Deharveng L., et al., 2012, *A&A*, **546**, A74
- Doi Y., et al., 2020, *ApJ*, **899**, 28
- Eswaraiiah C., et al., 2020, *ApJ*, **897**, 90
- Eswaraiiah C., et al., 2021, *The Astrophysical Journal Letters*, **912**, L27
- Federrath C., 2015, *Monthly Notices of the Royal Astronomical Society*, **450**, 4035
- Federrath C., Klessen R. S., 2012, *The Astrophysical Journal*, **761**, 156
- Fiege J. D., Pudritz R. E., 2000, *MNRAS*, **311**, 85
- Friberg P., Bastien P., Berry D., Savini G., Graves S. F., Pattle K., 2016, in Holland W. S., Zmuidzinas J., eds, *Society of Photo-Optical Instrumentation Engineers (SPIE) Conference Series Vol. 9914, Millimeter, Submillimeter, and Far-Infrared Detectors and Instrumentation for Astronomy VIII*. p. 991403, doi:10.1117/12.2231943
- Girart J. M., Rao R., Marrone D. P., 2006, *Science*, **313**, 812
- Girart J. M., Beltrán M. T., Zhang Q., Rao R., Estalella R., 2009, *Science*, **324**, 1408
- Girart J. M., Frau P., Zhang Q., Koch P. M., Qiu K., Tang Y.-W., Lai S.-P., Ho P. T. P., 2013, *The Astrophysical Journal*, **772**, 69
- Gómez G. C., Vázquez-Semadeni E., 2014, *ApJ*, **791**, 124
- Gómez G. C., Vázquez-Semadeni E., Zamora-Avilés M., 2018, *MNRAS*, **480**, 2939
- Gómez G. C., Vázquez-Semadeni E., Palau A., 2021, *MNRAS*, **502**, 4963
- Gutermuth R. A., Megeath S. T., Myers P. C., Allen L. E., Pipher J. L., Fazio G. G., 2009, *ApJS*, **184**, 18
- Harvey P. M., et al., 2008, *ApJ*, **680**, 495
- Heitsch F., Zweibel E. G., Mac Low M.-M., Li P., Norman M. L., 2001, *ApJ*, **561**, 800
- Hennebelle P., 2018, *A&A*, **611**, A24
- Hennebelle P., Falgarone E., 2012, *A&ARv*, **20**, 55
- Hennebelle P., Inutsuka S.-i., 2019, *Frontiers in Astronomy and Space Sciences*, **6**
- Hildebrand R. H., Kirby L., Dotson J. L., Houde M., Vaillancourt J. E., 2009, *ApJ*, **696**, 567
- Hoang T., Lazarian A., 2008, *MNRAS*, **388**, 117
- Hoang T., Lazarian A., 2014, *MNRAS*, **438**, 680
- Holland W. S., et al., 2013, *MNRAS*, **430**, 2513
- Houde M., Vaillancourt J. E., Hildebrand R. H., Chitsazzadeh S., Kirby L., 2009, *ApJ*, **706**, 1504
- Hull C. L. H., et al., 2017, *ApJ*, **847**, 92
- Hwang J., et al., 2022, *ApJ*, **941**, 51
- Kauffmann J., Bertoldi F., Bourke T. L., Evans N. J. I., Lee C. W., 2008, *A&A*, **487**, 993
- Kauffmann J., Pillai T., Goldsmith P. F., 2013, *ApJ*, **779**, 185

- Klessen R. S., Glover S. C. O., 2016, in Revaz Y., Jablonka P., Teyssier R., Mayer L., eds, Saas-Fee Advanced Course Vol. 43, Saas-Fee Advanced Course. p. 85 ([arXiv:1412.5182](https://arxiv.org/abs/1412.5182)), doi:10.1007/978-3-662-47890-5_2
- Klessen R. S., Heitsch F., Low M.-M. M., 2000, *The Astrophysical Journal*, 535, 887
- Koch P. M., Tang Y.-W., Ho P. T. P., 2012a, *ApJ*, 747, 79
- Koch P. M., Tang Y.-W., Ho P. T. P., 2012b, *ApJ*, 747, 80
- Koch P. M., Tang Y.-W., Ho P. T. P., 2013, *ApJ*, 775, 77
- Koch P. M., et al., 2014, *The Astrophysical Journal*, 797, 99
- Kumar M. S. N., Palmeirim P., Arzoumanian D., Inutsuka S. I., 2020, *A&A*, 642, A87
- Kumar M. S. N., Arzoumanian D., Men'shchikov A., Palmeirim P., Matsumura M., Inutsuka S., 2022, *A&A*, 658, A114
- Kwon J., et al., 2018, *ApJ*, 859, 4
- Lazarian A., 2007, *J. Quant. Spectrosc. Radiative Transfer*, 106, 225
- Li H.-b., Houde M., 2008, *ApJ*, 677, 1151
- Li H. B., Goodman A., Sridharan T. K., Houde M., Li Z. Y., Novak G., Tang K. S., 2014, in Beuther H., Klessen R. S., Dullemond C. P., Henning T., eds, Protostars and Planets VI. pp 101–123 ([arXiv:1404.2024](https://arxiv.org/abs/1404.2024)), doi:10.2458/azu_uapress_9780816531240-ch005
- Lin S.-J., et al., 2023, [arXiv e-prints](https://arxiv.org/abs/2311.08026), p. [arXiv:2311.08026](https://arxiv.org/abs/2311.08026)
- Liu H. B., Galván-Madrid R., Jiménez-Serra I., Román-Zúñiga C., Zhang Q., Li Z., Chen H.-R., 2015, *ApJ*, 804, 37
- Liu J., et al., 2019, *ApJ*, 877, 43
- Liu J., Zhang Q., Qiu K., Liu H. B., Pillai T., Girart J. M., Li Z.-Y., Wang K., 2020, *ApJ*, 895, 142
- Liu J., Zhang Q., Qiu K., 2022, *Frontiers in Astronomy and Space Sciences*, 9, 943556
- Mac Low M.-M., Klessen R. S., 2004, *Reviews of Modern Physics*, 76, 125
- Mairs S., et al., 2021, *The Astronomical Journal*, 162, 191
- Mao S. A., Ostriker E. C., Kim C.-G., 2020, *ApJ*, 898, 52
- Molinari S., et al., 2010, *A&A*, 518, L100
- Mouschovias T. C., Tassis K., Kunz M. W., 2006, *ApJ*, 646, 1043
- Myers P. C., 2009, *ApJ*, 700, 1609
- Nakamura F., Li Z.-Y., 2008, *The Astrophysical Journal*, 687, 354
- Naranjo-Romero R., Zapata L. A., Vázquez-Semadeni E., Takahashi S., Palau A., Schilke P., 2012, *ApJ*, 757, 58
- Ostriker E. C., Stone J. M., Gammie C. F., 2001, *ApJ*, 546, 980
- Padoan P., Nordlund Å., 2002, *ApJ*, 576, 870
- Padoan P., Goodman A., Draine B. T., Juvela M., Nordlund Å., Rögnvaldsson Ö. E., 2001, *ApJ*, 559, 1005
- Pattle K., et al., 2017, *ApJ*, 846, 122
- Pattle K., et al., 2018, *The Astrophysical Journal Letters*, 860, L6
- Pattle K., et al., 2019, *The Astrophysical Journal*, 880, 27
- Pattle K., Fissel L., Tahani M., Liu T., Ntormousi E., 2022, [arXiv e-prints](https://arxiv.org/abs/2203.11179), p. [arXiv:2203.11179](https://arxiv.org/abs/2203.11179)
- Peretto N., et al., 2014, *A&A*, 561, A83
- Pillai T., Kauffmann J., Wyrowski F., Hatchell J., Gibb A. G., Thompson M. A., 2011, *A&A*, 530, A118
- Pillai T. G. S., et al., 2020, *Nature Astronomy*, 4, 1195
- Planck Collaboration et al., 2016, *A&A*, 586, A138
- Planck Collaboration et al., 2020, *A&A*, 641, A12
- Rawat V., et al., 2023, *MNRAS*, 521, 2786
- Rawat V., et al., 2024, The Giant Molecular Cloud G148.24+00.41: Gas Properties, Kinematics, and Cluster Formation at the Nexus of Filamentary Flows ([arXiv:2401.03202](https://arxiv.org/abs/2401.03202))
- Sadavoy S. I., et al., 2018, *ApJ*, 869, 115
- Salvatier J., Wiecki T. V., Fonnesbeck C., 2016, *PeerJ Computer Science*, 2, e55
- Sanhueza P., Jackson J. M., Zhang Q., Guzmán A. E., Lu X., Stephens I. W., Wang K., Tatematsu K., 2017, *The Astrophysical Journal*, 841, 97
- Schisano E., et al., 2020, *MNRAS*, 492, 5420
- Seifried D., Walch S., 2015, *MNRAS*, 452, 2410
- Shan W., et al., 2012, *IEEE Transactions on Terahertz Science and Technology*, 2, 593
- Shimajiri Y., André P., Palmeirim P., Arzoumanian D., Bracco A., Könyves V., Ntormousi E., Ladjelate B., 2019, *A&A*, 623, A16
- Soam A., et al., 2018, *ApJ*, 861, 65
- Soam A., et al., 2019, *ApJ*, 883, 95
- Soler J. D., Hennebelle P., Martin P. G., Miville-Deschênes M. A., Netterfield C. B., Fissel L. M., 2013, *ApJ*, 774, 128
- Soler J. D., et al., 2017, *A&A*, 603, A64
- Su Y., et al., 2019, *The Astrophysical Journal Supplement Series*, 240, 9
- Tan J. C., Kong S., Butler M. J., Caselli P., Fontani F., 2013, *ApJ*, 779, 96
- Tang Y.-W., Ho P. T. P., Koch P. M., Guilloteau S., Dutrey A., 2013, *ApJ*, 763, 135
- Tang Y.-W., Koch P. M., Peretto N., Novak G., Duarte-Cabral A., Chapman N. L., Hsieh P.-Y., Yen H.-W., 2019, *ApJ*, 878, 10
- Treviño-Morales S. P., et al., 2019, *A&A*, 629, A81
- Vaillancourt J. E., 2006, *PASP*, 118, 1340
- Vázquez-Semadeni E., Palau A., Ballesteros-Paredes J., Gómez G. C., Zamora-Avilés M., 2019, *MNRAS*, 490, 3061
- Wang J.-W., et al., 2019, *ApJ*, 876, 42
- Wang J.-W., Lai S.-P., Clemens D. P., Koch P. M., Eswarajah C., Chen W.-P., Pandey A. K., 2020a, *ApJ*, 888, 13
- Wang J.-W., Koch P. M., Galván-Madrid R., Lai S.-P., Liu H. B., Lin S.-J., Pattle K., 2020b, *ApJ*, 905, 158
- Wang J.-W., et al., 2022, *ApJ*, 931, 115
- Ward-Thompson D., et al., 2017, *ApJ*, 842, 66
- Whittet D. C. B., Hough J. H., Lazarian A., Hoang T., 2008, *ApJ*, 674, 304
- Zamora-Avilés M., Ballesteros-Paredes J., Hartmann L. W., 2017, *Monthly Notices of the Royal Astronomical Society*, 472, 647
- Zavagno A., et al., 2023, *A&A*, 669, A120
- Zhang Q., et al., 2014, *ApJ*, 792, 116

APPENDIX A: INTENSITY GRADIENTS VERSUS LOCAL GRAVITATIONAL FIELD

Fig. A1a shows the relative orientations of intensity gradient and local gravity, and Fig. A1b shows the distribution of the angular difference between their orientations, i.e. $\Delta\theta_{IG, LG}$. Similar to $\Delta\theta_{B, IG}$ and $\Delta\theta_{B, LG}$, the correlation between the angles (θ_{IG} and θ_{LG}) is better in the CC and WC regions in comparison to NES region.

This paper has been typeset from a $\text{\TeX}/\text{\LaTeX}$ file prepared by the author.

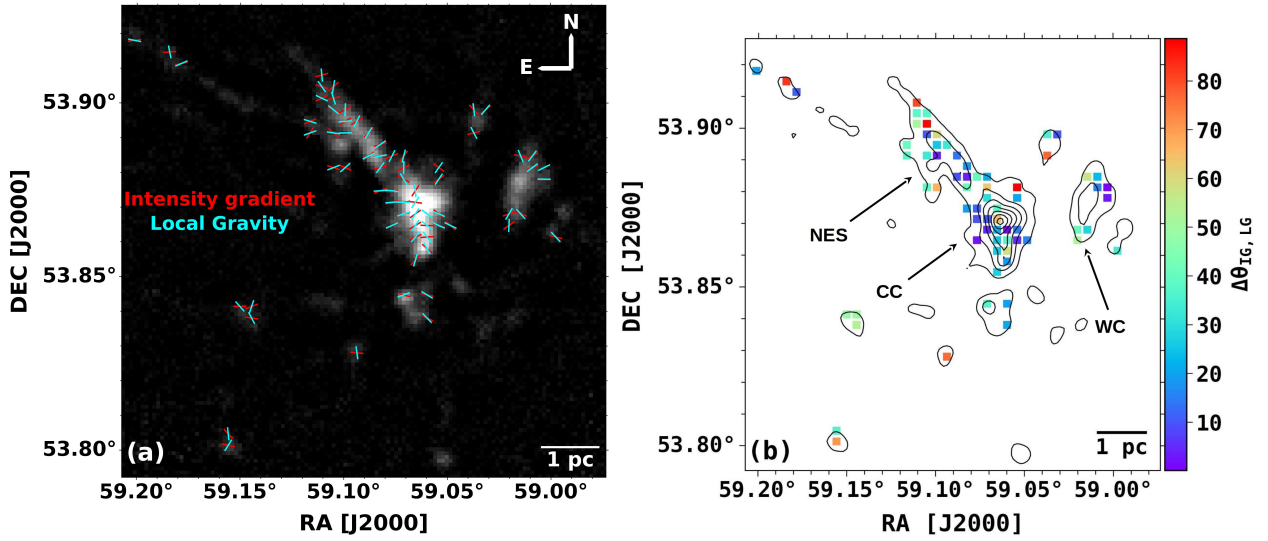


Figure A1. (a) The orientations of the intensity gradients (red segments) and local gravity (cyan vectors) are overlaid on the 850 μm Stokes I map. (b) The distribution of the offset between the position angles of the intensity gradients and local gravity, i.e., $\Delta\theta_{IG, LG} = |(\theta_{IG} - \theta_{LG})|$ over the contours of 850 μm Stokes I map. The contour levels are same as in Fig. 2.